JACS
JOURNAL OF THE AMERICAN CHEMICAL SOCIETY
Communication
Cite This: J. Am. Chem. Soc. 2018, 140, 14590−14594
pubs.acs.org/JACS

A Redox-Switchable, Allosteric Coordination Complex

Ho Fung Cheng,[†] Andrea I. d'Aquino,[†] Joaquín Barroso-Flores,[‡] and Chad A. Mirkin*[,†]

[†]Department of Chemistry and International Institute for Nanotechnology, Northwestern University, 2145 Sheridan Road, Evanston, Illinois 60208-3113, United States

[‡]Centro Conjunto de Investigación en Química Sustentable, UAEM-UNAM, Carretera Toluca-Atlacomulco Km 14.5, Personal de la UNAM, Unidad San Cayetano, Toluca, Estado de México C.P. 50200, Mexico

Supporting Information

ABSTRACT: A redox-regulated molecular tweezer complex was synthesized via the weak-link approach. The Pt^{II} complex features a redox-switchable hemilabile ligand (RHL) functionalized with a ferrocenyl moiety, whose oxidation state modulates the opening of a specific coordination site. Allosteric regulation by redox agents gives reversible access to two distinct structural states—a fully closed state and a semi-open state—whose interconversion was studied via multinuclear NMR spectroscopy, cyclic voltammetry, and UV−vis−NIR spectroscopy. Two structures in this four-state system were further characterized via SCXRD, while the others were modeled through DFT calculations. This fully reversible, RHL-based system defines an unusual level of electrochemical control over the occupancy of a specific coordination site, thereby providing access to four distinct coordination states within a single system, each defined and differentiated by structure and oxidation state.

Opening and closing a coordination site is a powerful way to control the electronic properties and steric environment of a metal center.[1−3] Coordination state regulation has shown promise in stoichiometric[4−6] and catalytic[7−10] reactions involving metal and metallo-supramolecular complexes. Therefore, driving the reversible and selective opening of a metal's coordination site using external stimuli is an attractive goal in organometallic and inorganic chemistry.

Electrons are among the most accessible and useful stimuli employed to modulate the lability of metal−ligand bonds[11] and the reactivity of metal centers.[12−15] Such modulation can occur at a structure-directing metal node[16−24] or a redox-active ligand.[11,25−33] The latter, which enables the control of coordination sites without changing the metal's formal oxidation state, underlies the premise of redox-switchable hemilabile ligands (RHLs).[11,25,26,33] RHLs contain a non-labile, anchoring heteroatom and a labile heteroatom whose donor strength changes as a function of the ligand oxidation state. However, achieving selective control over a single coordination site using RHLs has been synthetically challenging. Designing RHLs that enable selective and fully reversible opening of a coordination site is non-trivial (Figure 1a),[25−27,34] and regulation can be hampered by the instability of the oxidized states,[35−37] the interference from multiple redox-active elements,[27] or the difficulty of studying open-shell species in solution.[36] Therefore, it would be a significant advance to develop a complex whose coordination site can be reversibly and selectively opened via electron transfer.

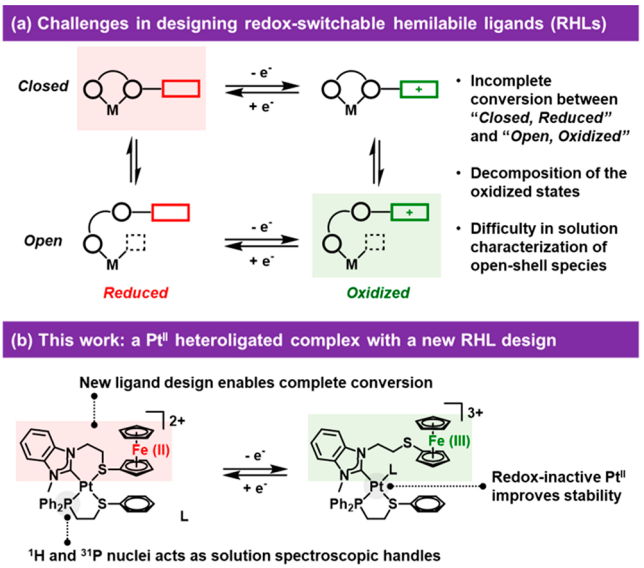

Figure 1. (a) Challenges in reversibly opening coordination sites via redox reactions. (b) A new redox-switchable complex design.

A promising strategy to synthesize structurally addressable coordination complexes with fine electronic and structural control is the weak-link approach (WLA).[38] The hemilabile ligands employed allow one to regulate the coordination state of substitutionally labile heteroatoms (the weak-link) using small-molecule and anionic effectors (e.g., halides, amines, carboxylates);[38] as such, the WLA has been used to develop stimuli-responsive catalysts,[39−41] host−guest cages,[42,43] polymeric materials,[44] and signal amplifiers.[45,46]

To address the challenges associated with designing RHLs (Figure 1a), we have identified three requirements for a WLA-based model system: (1) The weak-link should be displaced by place-holding exogenous ligands only when the RHL is oxidized. (2) The structure-directing metal node should be redox-inactive. (3) The complex should possess spectroscopic handles for facile structure characterization in solution.

Based on these requirements, we designed a Pt^{II} heteroligated WLA tweezer complex containing a novel RHL (Figure 1b). We

Received: August 29, 2018
Published: October 26, 2018

DOI: 10.1021/jacs.8b09321
J. Am. Chem. Soc. 2018, 140, 14590−14594

chose to employ a redox-inactive Pt^{II} node to avoid instability of the oxidized states previously observed in Rh^{I} complexes possessing RHLs.[35,36] The Pt^{II} heteroligated complex can be formed by the stepwise assembly of an N-heterocyclic carbene-thioether (NHC,S) ligand and a phosphino-thioether (P,S) ligand.[47] The non-labile NHC-Pt bond anchors the RHL to the metal node and prevents undesirable ligand scrambling,[47] while the ^{31}P nuclei provides a spectroscopic handle for facile structure characterization.[48,49] To enable complete, redox-driven interconversion between two coordination states, the RHL incorporates a ferrocenyl-bound thioether (S-Fc) as part of the NHC,S chelate, which possesses a weaker Pt−S bond than a P,S chelate.[43] We hypothesized that, upon oxidation, the binding affinity of S-Fc^{+} would be sufficiently weakened,[35] allowing exogenous ligands to specifically displace that thioether and occupy the corresponding coordination site.

Transmetalation of the RHL precursor **1** with 0.5 equiv of silver(I) oxide (Ag_2O) and 1 equiv of dichloro(1,5-cyclooctadiene)platinum(II) ($PtCl_2$(cod)) gave the monoligated complex **2**, which was combined with 1 equiv of (2-(phenylthio)ethyl)diphenylphosphine to form the fully open heteroligated complex **3** (Figure 2). Subsequent chloride

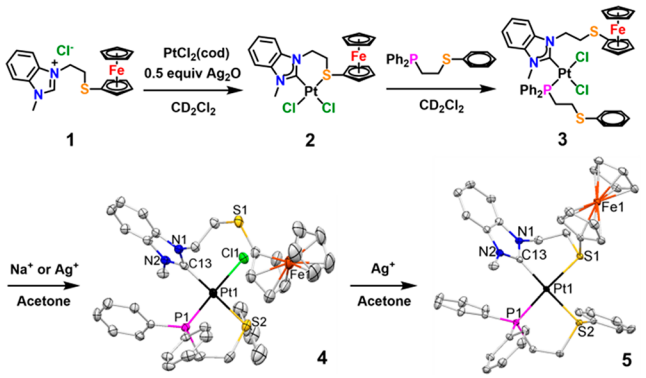

Figure 2. Synthesis and crystal structures of semi-open complex **4** and fully closed complex **5** (50% probability ellipsoids). Counteranions and solvent molecules are omitted for clarity.

abstractions resulted in the semi-open complex **4** and the fully closed complex **5**. Each compound was characterized by multinuclear NMR spectroscopy and high-resolution mass spectrometry (HRMS) (see the Supporting Information (SI)). In particular, the ^{31}P NMR spectrum of **5** (Figure S2) exhibited a downfield resonance (41.62 ppm) characteristic of a phosphine in a five-membered chelate,[49] and the small coupling constant ($^{1}J_{P-Pt}$ = 3183 Hz) indicates that the phosphine is *trans* to a thioether,[47] consistent with the fully closed structure. Density Functional Theory (DFT) calculations, carried out at the ω-B97XD/lanl2dz level of theory, were used to investigate the structure and the electronic properties of these complexes (see the SI). Comparing the diastereomers of **5**, a 1.59 kcal/mol energy difference was found (Table S4), deeming them isoenergetic. The presence of the second diastereomer was confirmed by an additional signal (37.50 ppm, $^{1}J_{P-Pt} \approx 3180$ Hz), which fully coalesced with the major signal at 343 K due to rapid diastereomer interconversion via thioether inversion (Figure S2).[47,50]

The solution-phase structures assigned to **1**, **2**, **4**, and **5** are consistent with the solid-state structures determined by single crystal X-ray diffraction (SCXRD) studies (Figures 2 and S28). The crystal structure of **5** showed that the NHC,S ligand and the P,S ligand chelate to the Pt^{II} center with a square planar geometry. The six-membered NHC,S chelate's bond angle approaches 90° at Pt^{II} (C13−Pt1−S1 = 88.26(6)°) and thus experiences less strain than the previously reported five-membered NHC,S chelate.[47] While the latter was opened by mild nucleophiles such as acetonitrile (MeCN) and thioanisole (PhSMe), we hypothesized that the former would not. Indeed, when a 10-fold excess of PhSMe was added to a solution of **5**, no reaction occurred as evidenced by ^{31}P NMR spectroscopy (Figure S3).

To understand how exogenous ligands affect the electronic properties of the RHL, complex **5** ($E_{1/2}$ = 0.38 V vs Fc/Fc^{+}) was studied by cyclic voltammetry (Figure 3). The peak separation

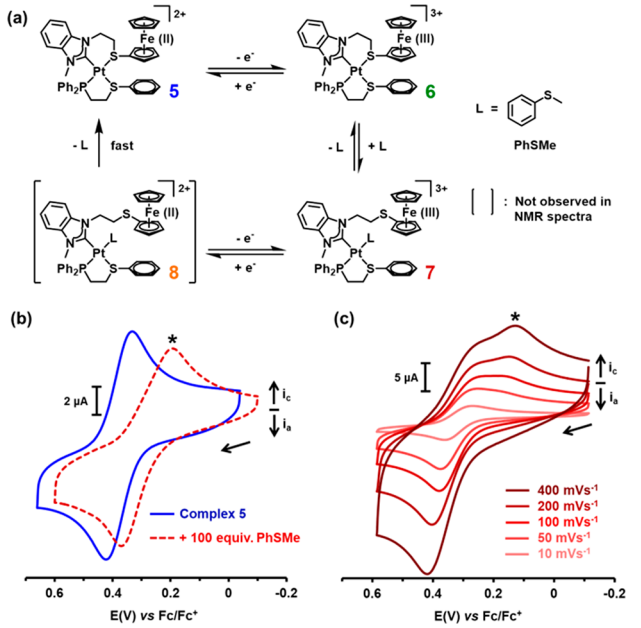

Figure 3. (a) Proposed electrochemical transformations for **5**. Cyclic voltammograms of **5** with (b) 0 and 100 equiv of PhSMe in 0.1 M $[nBu_4N][PF_6]/CH_2Cl_2$ at 50 mV s^{-1}, and (c) 10 equiv of PhSMe recorded at different scan rates.

increased from 0.09 to 0.18 V after adding 100 equiv of PhSMe. The cathodic peak associated with the reduction of Fe^{III} shifted by 0.14 V to a less positive potential (*, Figure 3b), suggesting that the oxidized RHL ligand underwent a coordination change that stabilizes Fe^{III} when exogenous ligands are present. Cyclic voltammograms of **5** with 10 equiv of PhSMe recorded at varying scan rates show that although there is one anodic wave associated with the conversion of **5** to **6**, there are two cathodic waves that can be detected at faster scan rates (Figure 3c). These waves are associated with the reduction of **6** and **7**, respectively, which are in equilibrium with one another, a slow process on the electrochemical time scale.[51,52] These observations are consistent with the proposed square scheme (Figure 3a),[53] in which the oxidized complex **6** is opened by PhSMe to form **7**, whose ferrocenium center is electronically stabilized by the relief of electrostatic repulsion between Pt^{II} and Fe^{III}. Upon reduction of **7** to give the transient species **8**, PhSMe is displaced quickly to re-form **5**.

With promising results from the electrochemical studies, we investigated whether the coordination state of **5** could be controlled with chemical redox agents. Thus, an orange solution of **5** in dichloromethane-d_2 (CD_2Cl_2) was treated with silver

DOI: 10.1021/jacs.8b09321
J. Am. Chem. Soc. 2018, 140, 14590−14594

tetrafluoroborate ($AgBF_4$) to yield a green solution that gradually formed a dark green precipitate, which was redissolved in nitromethane-d_3 (CD_3NO_2) for characterization. The formation of S-Fc$^+$ in oxidized complex **6** was substantiated by the ligand-to-metal charge-transfer (LMCT) band at 665 nm (Figure 4a), characteristic of a ferrocenium substituted with

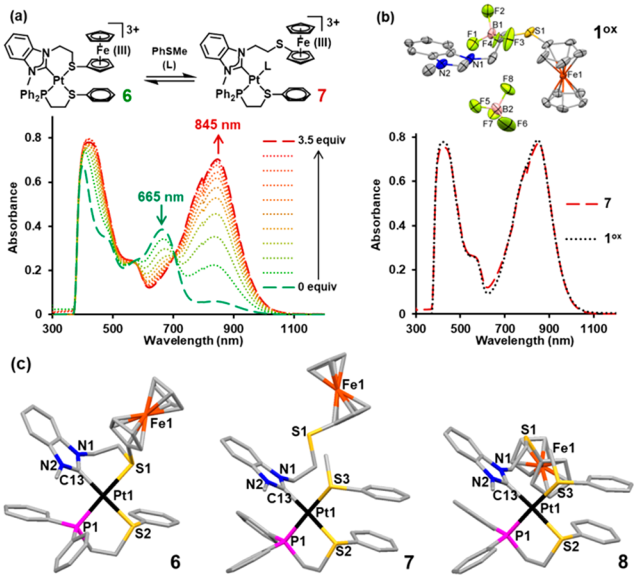

Figure 4. (a) UV−vis−NIR spectra of **6** titrated with PhSMe to form **7**. (b) Crystal structure of **1**^{ox} drawn with 50% probability ellipsoids. UV−vis−NIR spectra of **1**^{ox} and **7** (5 equiv of PhSMe). (c) Energy-minimized models of **6**, **7**, and **8**.

electron donating groups.[54] To test the hypothesis that mild nucleophiles open the oxidized complex, PhSMe was titrated to a solution of **6** to give a reddish brown solution. Ultraviolet−visible−near-infrared (UV−vis−NIR) spectroscopy revealed isosbestic points at 507 and 705 nm, consistent with the proposed two-state equilibrium between **6**, PhSMe, and **7** (Figure 4a). Using the absorbance of the red-shifted band (845 nm) that increases with the concentration of PhSMe, binding isotherms (Figure S25) were constructed and fitted to a 1:1 binding model to afford the association constant (K_a = 1881 ± 1 M^{-1}).[55] Importantly, **7** has a spectrum identical to that of the oxidized RHL ligand precursor (**1**^{ox}), whose structure was verified by SCXRD studies (Figure 4b), supporting the hypothesis that **7** possesses a non-coordinating S-Fc$^+$ displaced from Pt^{II} by PhSMe.

Comparison between the energy-minimized models of the oxidized, semi-open complex **7** and its non-oxidized counterpart **8** (Figure 4c) revealed that electrostatic repulsion leads to an extended ligand conformation that could be detected by NMR spectroscopy. Upon conversion from **6** to **7**, the distance between the paramagnetic Fe^{III} center and the ^{31}P nuclei increases by ∼2.3 Å (Table S5). Since paramagnetic relaxation enhancement has a distance dependence of $\langle r^{-6} \rangle$,[56] conversion to **7** should result in sharper ^{31}P signals,[34] but the ^{1}H signals of S-Fc$^+$ should remain broadened and isotropically shifted to the downfield region.[57] Confirming our predictions, the ^{31}P NMR spectrum of **7** sharpened significantly (Figure 5d) compared to that of **6** (Figure 5c), while the ^{1}H NMR spectrum continued to exhibit broad, downfield signals. In addition, the magnetically inequivalent protons of S-Fc$^+$ became relatively well-resolved in the ^{1}H NMR spectrum of **7**, showing the expected integral ratio

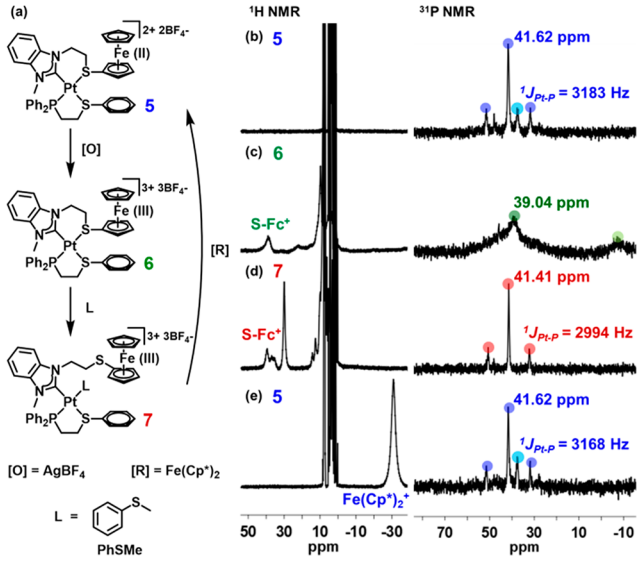

Figure 5. (a) Interconversion of **5**, **6**, and **7**. ^{1}H NMR (CD_3NO_2) and ^{31}P NMR (CD_3NO_2) spectra of (b) **5**, after addition of (c) $AgBF_4$, (d) PhSMe, and (e) Fe(Cp*)$_2$.

of ∼2:2:5 (Figure S56). This spectral resolution was only observed among species with a non-coordinated, conformationally flexible S-Fc$^+$ group (Figure S10).

Comparison between the ^{31}P NMR spectra of **5** and **7** (Figure 5b,d) confirmed that they represent different species. The ^{31}P NMR spectrum of **7** exhibited a slightly upfield resonance (41.41 ppm), a smaller coupling constant ($^1J_{P-Pt}$ = 2994 Hz), and, crucially, no signs of diastereomers—consistent with the formation of a semi-open complex. Reduction of **7** by decamethylferrocene Fe(Cp*)$_2$ re-formed **5** as evidenced by the ^{1}H and ^{31}P NMR spectra (Figure 5e). Concurrent ^{1}H diffusion-ordered spectroscopy (DOSY) experiments showed that the diffusion coefficient of PhSMe increased significantly upon addition of Fe(Cp*)$_2$ (Table S1), indicating that PhSMe only associates with the oxidized complex **6** to form **7** and diffuses more freely upon reduction of **7**.

One-pot allosteric regulation can be achieved using oxidants whose reduction potentials are less affected by the presence of nucleophiles.[58] For example, the oxidant $[N(C_6H_4Br\text{-}4)_3]^+BF_4^-$ was prepared in situ and added to a mixture of **5** and PhSMe in CD_2Cl_2. Expected changes in ^{31}P NMR spectrum (Figure S7c) were observed—an upfield resonance shift (39.48 ppm), a smaller coupling constant ($^1J_{P-Pt}$ = 3043 Hz), and the disappearance of the diastereomeric signal. Together with the downfield signals in the ^{1}H NMR spectrum, this evidence confirmed that **5** was converted to **7**, which can be reduced by Fe(Cp*)$_2$ to regenerate **5** (Figure S7).

Finally, it is important to consider whether the system design meets our initial criteria. First, the redox-inactive Pt^{II} node prevented degradation of the oxidized complexes. UV−vis−NIR spectrum of **7** showed no signs of decomposition over 36 h (Figure S26). Second, distal electron transfer modulated the lability of the Fc-bound thioether. DFT calculations estimated that the Pt−S bond weakens by 5.66 kcal/mol after RHL oxidation (Table S5). Third, an exogenous ligand with appropriate nucleophilicity was essential to achieving selective regulation. A large excess of weak nucleophiles such as MeCN was required for complete conversion to the semi-open state (Figure S8). Strong nucleophiles such as tetrahydrothiophene,

DOI: 10.1021/jacs.8b09321
J. Am. Chem. Soc. 2018, 140, 14590−14594

however, led to indiscriminate opening of both **5** and **6** (Figure S9). Fourth, strategic placement of the redox-responsive group was critical in ensuring complete opening of a coordination site upon redox reaction. If Fc were attached to the thioether of a P,S ligand, the resulting oxidized complex could only undergo partial conversion to the semi-open state (Figure S6).

In conclusion, this work lays the foundation for developing systems where one can drive the reversible opening and closing of targeted coordination sites using electron-transfer reactions. Such control will be useful for activating and deactivating catalytic structures[11,32,34] and opens avenues to the development of sophisticated allosteric protein mimics[39,41] that can be selectively regulated by electrochemical methods.

■ ASSOCIATED CONTENT

Supporting Information

The Supporting Information is available free of charge on the ACS Publications website at DOI: 10.1021/jacs.8b09321.

Synthetic procedures, spectral data, titration and electrochemical studies, and crystallographic and computational information, including Figures S1−S67 and Tables S1−S5 (PDF)

Crystallographic data for **1** (CCDC 1862235) (CIF)

Crystallographic data for $\mathbf{1}^{ox}$ (CCDC 1862236) (CIF)

Crystallographic data for **2** (CCDC 1862237) (CIF)

Crystallographic data for **4** (CCDC 1862238) (CIF)

Crystallographic data for **5** (CCDC 1862239) (CIF)

■ AUTHOR INFORMATION

Corresponding Author

*chadnano@northwestern.edu

ORCID

Ho Fung Cheng: 0000-0003-2580-0912

Andrea I. d'Aquino: 0000-0002-4204-8219

Joaquín Barroso-Flores: 0000-0003-0554-7569

Chad A. Mirkin: 0000-0002-6634-7627

Notes

The authors declare no competing financial interest.

■ ACKNOWLEDGMENTS

This material is based upon work supported by the following awards: National Science Foundation grant CHE-1709888, U.S. Army grant W911NF-15-1-0151, and the Vannevar Bush Faculty Fellowship program sponsored by the Basic Research Office of the Assistant Secretary of Defense for Research and Engineering and funded by the Office of Naval Research through grant N00014-15-1-0043. This work made use of instruments of IMSERC at Northwestern University that have received support from the Soft and Hybrid Nanotechnology Experimental (SHyNE) Resource (NSF ECCS-1542205), the State of Illinois, and International Institute for Nanotechnology (IIN). A.I.D. acknowledges a National Science Foundation Graduate Research Fellowship. We also thank DGTIC-UNAM for granting access to their supercomputing facilities known as "Miztli".

■ REFERENCES

(1) Slone, C. S.; Weinberger, D. A.; Mirkin, C. A. The transition metal coordination chemistry of hemilabile ligands. *Prog. Inorg. Chem.* **2007**, *48*, 233−350.

(2) Braunstein, P.; Naud, F. Hemilability of hybrid ligands and the coordination chemistry of oxazoline-based systems. *Angew. Chem., Int. Ed.* **2001**, *40*, 680−699.

(3) Morris, R. E.; Brammer, L. Coordination change, lability and hemilability in metal-organic frameworks. *Chem. Soc. Rev.* **2017**, *46*, 5444−5462.

(4) Weinberger, D. A.; Higgins, T. B.; Mirkin, C. A.; Stern, C. L.; Liable-Sands, L. M.; Rheingold, A. L. Terthienyl and Poly-terthienyl Ligands as Redox-Switchable Hemilabile Ligands for Oxidation-State-Dependent Molecular Uptake and Release. *J. Am. Chem. Soc.* **2001**, *123*, 2503−2516.

(5) Angell, S. E.; Rogers, C. W.; Zhang, Y.; Wolf, M. O.; Jones, W. E. Hemilabile coordination complexes for sensing applications. *Coord. Chem. Rev.* **2006**, *250*, 1829−1841.

(6) Rebilly, J.-N.; Colasson, B.; Bistri, O.; Over, D.; Reinaud, O. Biomimetic cavity-based metal complexes. *Chem. Soc. Rev.* **2015**, *44*, 467−489.

(7) Bader, A.; Lindner, E. Coordination chemistry and catalysis with hemilabile oxygen-phosphorus ligands. *Coord. Chem. Rev.* **1991**, *108*, 27−110.

(8) Lyaskovskyy, V.; de Bruin, B. Redox Non-Innocent Ligands: Versatile New Tools to Control Catalytic Reactions. *ACS Catal.* **2012**, *2*, 270−279.

(9) Blanco, V.; Leigh, D. A.; Marcos, V. Artificial switchable catalysts. *Chem. Soc. Rev.* **2015**, *44*, 5341−5370.

(10) Miller, A. J. M. Controlling ligand binding for tunable and switchable catalysis: cation-modulated hemilability in pincer-crown ether ligands. *Dalton Trans.* **2017**, *46*, 11987−12000.

(11) Allgeier, A. M.; Mirkin, C. A. Ligand design for electrochemically controlling stoichiometric and catalytic reactivity of transition metals. *Angew. Chem., Int. Ed.* **1998**, *37*, 894−908.

(12) Gregson, C. K. A.; Gibson, V. C.; Long, N. J.; Marshall, E. L.; Oxford, P. J.; White, A. J. P. Redox Control within Single-Site Polymerization Catalysts. *J. Am. Chem. Soc.* **2006**, *128*, 7410−7411.

(13) Broderick, E. M.; Guo, N.; Vogel, C. S.; Xu, C.; Sutter, J.; Miller, J. T.; Meyer, K.; Mehrkhodavandi, P.; Diaconescu, P. L. Redox Control of a Ring-Opening Polymerization Catalyst. *J. Am. Chem. Soc.* **2011**, *133*, 9278−9281.

(14) Magenau, A. J. D.; Strandwitz, N. C.; Gennaro, A.; Matyjaszewski, K. Electrochemically Mediated Atom Transfer Radical Polymerization. *Science* **2011**, *332*, 81−84.

(15) Biernesser, A. B.; Li, B.; Byers, J. A. Redox-Controlled Polymerization of Lactide Catalyzed by Bis(imino)pyridine Iron Bis(alkoxide) Complexes. *J. Am. Chem. Soc.* **2013**, *135*, 16553−16560.

(16) Bowyer, W. J.; Geiger, W. E. Structural consequences of electron-transfer reactions. 11. Electrochemically induced changes in hapticity in mixed-sandwich compounds of iridium and rhodium. *J. Am. Chem. Soc.* **1985**, *107*, 5657−5663.

(17) Kuchynka, D. J.; Kochi, J. K. Facile rearrangement and electron transfer of 19-electron radicals from the reduction of the bischelated manganese carbonyl cation $Mn(CO)_2[PPh_2(CH_2)_2PPh_2]_2^+$. *Inorg. Chem.* **1988**, *27*, 2574−2581.

(18) Zahn, S.; Canary, J. W. Redox-switched exciton-coupled circular dichroism: A novel strategy for binary molecular switching. *Angew. Chem., Int. Ed.* **1998**, *37*, 305−307.

(19) Al-Sayah, M. H.; Branda, N. R. Controlling allostery using redox chemistry. *Chem. Commun.* **2002**, 178−179.

(20) Canary, J. W. Redox-triggered chiroptical molecular switches. *Chem. Soc. Rev.* **2009**, *38*, 747−756.

(21) Lee, Y.; Mankad, N. P.; Peters, J. C. Triggering N_2 uptake via redox-induced expulsion of coordinated NH_3 and N_2 silylation at trigonal bipyramidal iron. *Nat. Chem.* **2010**, *2*, 558−565.

(22) Le Poul, N.; Le Mest, Y.; Jabin, I.; Reinaud, O. Supramolecular Modeling of Mono-copper Enzyme Active Sites with Calix[6]arene-based Funnel Complexes. *Acc. Chem. Res.* **2015**, *48*, 2097−2106.

(23) Kriegel, B. M.; Naested, L. C. E.; Nocton, G.; Lakshmi, K. V.; Lohrey, T. D.; Bergman, R. G.; Arnold, J. Redox-Initiated Reactivity of Dinuclear β-Diketiminatoniobium Imido Complexes. *Inorg. Chem.* **2017**, *56*, 1626−1637.

DOI: 10.1021/jacs.8b09321
J. Am. Chem. Soc. 2018, 140, 14590−14594

(24) Arnett, C. H.; Chalkley, M. J.; Agapie, T. A Thermodynamic Model for Redox-Dependent Binding of Carbon Monoxide at Site-Differentiated, High Spin Iron Clusters. *J. Am. Chem. Soc.* **2018**, *140*, 5569−5578.
(25) Singewald, E. T.; Mirkin, C. A.; Stern, C. L. A redox-switchable hemilabile ligand: electrochemical control of the coordination environment of a Rh^{I} complex. *Angew. Chem., Int. Ed. Engl.* **1995**, *34*, 1624−1627.
(26) Sembiring, S. B.; Colbran, S. B.; Craig, D. C. Complexes of New Electrochemically-Active p-Quinonyl-/p-hydroquinonylphosphines: Multiple Electron/Proton Transfer Reactions and Electrochemical/pH Control of p-Quinonyl-/p-Hydroquinonyl o-Oxygen Atom Coordination. *Inorg. Chem.* **1995**, *34*, 761−762.
(27) He, Z.; Colbran, S. B.; Craig, D. C. Could redox-switched binding of a redox-active ligand to a copper(II) center drive a conformational proton pump gate? A synthetic model study. *Chem. - Eur. J.* **2003**, *9*, 116−129.
(28) Ringenberg, M. R.; Kokatam, S. L.; Heiden, Z. M.; Rauchfuss, T. B. Redox-Switched Oxidation of Dihydrogen Using a Non-Innocent Ligand. *J. Am. Chem. Soc.* **2008**, *130*, 788−789.
(29) Huebner, R.; Weber, S.; Strobel, S.; Sarkar, B.; Zalis, S.; Kaim, W. Reversible Intramolecular Single-Electron Oxidative Addition Involving a Hemilabile Noninnocent Ligand. *Organometallics* **2011**, *30*, 1414−1418.
(30) Bubrin, M.; Schweinfurth, D.; Ehret, F.; Zalis, S.; Kvapilova, H.; Fiedler, J.; Zeng, Q.; Hartl, F.; Kaim, W. Structure and Spectroelectrochemical Response of Arene-Ruthenium and Arene-Osmium Complexes with Potentially Hemilabile Noninnocent Ligands. *Organometallics* **2014**, *33*, 4973−4985.
(31) Paretzki, A.; Bubrin, M.; Fiedler, J.; Zalis, S.; Kaim, W. Correlated Coordination and Redox Activity of a Hemilabile Noninnocent Ligand in Nickel Complexes. *Chem. - Eur. J.* **2014**, *20*, 5414−5422.
(32) Kaim, W.; Paretzki, A. Interacting metal and ligand based open shell systems: Challenges for experiment and theory. *Coord. Chem. Rev.* **2017**, *344*, 345−354.
(33) Das, S.; Sinha, S.; Jash, U.; Sikari, R.; Saha, A.; Barman, S. K.; Brandao, P.; Paul, N. D. Redox-Induced Interconversion and Ligand-Centered Hemilability in Ni^{II} Complexes of Redox-Noninnocent Azo-Aromatic Pincers. *Inorg. Chem.* **2018**, *57*, 5830−5841.
(34) Slone, C. S.; Mirkin, C. A.; Yap, G. P. A.; Guzei, I. A.; Rheingold, A. L. Oxidation-State-Dependent Reactivity and Catalytic Properties of a Rh(I) Complex Formed From a Redox-Switchable Hemilabile Ligand. *J. Am. Chem. Soc.* **1997**, *119*, 10743−10753.
(35) Allgeier, A. M.; Slone, C. S.; Mirkin, C. A.; Liable-Sands, L. M.; Yap, G. P. A.; Rheingold, A. Electrochemically Controlling Ligand Binding Affinity for Transition Metals via RHLs: The Importance of Electrostatic Effects. *J. Am. Chem. Soc.* **1997**, *119*, 550−559.
(36) Kourkine, I. V.; Slone, C. S.; Mirkin, C. A.; Liable-Sands, L. M.; Rheingold, A. L. Small Molecule-Induced Intramolecular Electron "Pitch and Catch" in a Rhodium(I) Complex with Substitutionally Inert Redox-Active Ligands. *Inorg. Chem.* **1999**, *38*, 2758−2759.
(37) Higgins, T. B.; Mirkin, C. A. Model compounds for polymeric redox-switchable hemilabile ligands. *Inorg. Chim. Acta* **1995**, *240*, 347−353.
(38) Lifschitz, A. M.; Rosen, M. S.; McGuirk, C. M.; Mirkin, C. A. Allosteric Supramolecular Coordination Constructs. *J. Am. Chem. Soc.* **2015**, *137*, 7252−7261.
(39) Yoon, H. J.; Kuwabara, J.; Kim, J. H.; Mirkin, C. A. Allosteric Supramolecular Triple-Layer Catalysts. *Science* **2010**, *330*, 66−69.
(40) McGuirk, C. M.; Mendez-Arroyo, J.; Lifschitz, A. M.; Mirkin, C. A. Allosteric Regulation of Supramolecular Oligomerization and Catalytic Activity via Coordination-Based Control of Competitive Hydrogen-Bonding Events. *J. Am. Chem. Soc.* **2014**, *136*, 16594−16601.
(41) Lifschitz, A. M.; Young, R. M.; Mendez-Arroyo, J.; Stern, C. L.; McGuirk, C. M.; Wasielewski, M. R.; Mirkin, C. A. An allosteric photoredox catalyst inspired by photosynthetic machinery. *Nat. Commun.* **2015**, *6*, 6541.
(42) Mendez-Arroyo, J.; Barroso-Flores, J.; Lifschitz, A. M.; Sarjeant, A. A.; Stern, C. L.; Mirkin, C. A. A Multi-State, Allosterically-Regulated Molecular Receptor With Switchable Selectivity. *J. Am. Chem. Soc.* **2014**, *136*, 10340−10348.
(43) Mendez-Arroyo, J.; d'Aquino, A. I.; Chinen, A. B.; Manraj, Y. D.; Mirkin, C. A. Reversible and Selective Encapsulation of Dextromethorphan and β-Estradiol Using an Asymmetric Molecular Capsule Assembled via the Weak-Link Approach. *J. Am. Chem. Soc.* **2017**, *139*, 1368−1371.
(44) d'Aquino, A. I.; Kean, Z. S.; Mirkin, C. A. Infinite Coordination Polymer Particles Composed of Stimuli-Responsive Coordination Complex Subunits. *Chem. Mater.* **2017**, *29*, 10284−10288.
(45) Gianneschi, N. C.; Nguyen, S. T.; Mirkin, C. A. Signal Amplification and Detection via a Supramolecular Allosteric Catalyst. *J. Am. Chem. Soc.* **2005**, *127*, 1644−1645.
(46) Yoon, H. J.; Mirkin, C. A. PCR-like Cascade Reactions in the Context of an Allosteric Enzyme Mimic. *J. Am. Chem. Soc.* **2008**, *130*, 11590−11591.
(47) Rosen, M. S.; Stern, C. L.; Mirkin, C. A. Heteroligated Pt^{II} Weak-Link Approach complexes using hemilabile N-heterocyclic carbene-thioether and phosphino-thioether ligands. *Chem. Sci.* **2013**, *4*, 4193−4198.
(48) Grim, S. O.; Keiter, R. L.; McFarlane, W. A phosphorus-31 nuclear magnetic resonance study of tertiary phosphine complexes of platinum(II). *Inorg. Chem.* **1967**, *6*, 1133−1137.
(49) Garrou, P. E. Δ_R Ring Contributions to ^{31}P NMR Parameters of Transition-Metal-Phosphorus Chelate Complexes. *Chem. Rev.* **1981**, *81*, 229−266.
(50) d'Aquino, A. I.; Cheng, H. F.; Barroso-Flores, J.; Kean, Z. S.; Mendez-Arroyo, J.; McGuirk, C. M.; Mirkin, C. A. An Allosterically Regulated, Four-State Macrocycle. *Inorg. Chem.* **2018**, *57*, 3568−3578.
(51) Nicholson, R. S.; Shain, I. Theory of stationary electrode polarography. Single scan and cyclic methods applied to reversible, irreversible, and kinetic systems. *Anal. Chem.* **1964**, *36*, 706−723.
(52) Bott, A. W. Characterization of chemical reactions coupled to electron transfer reactions using cyclic voltammetry. *Curr. Sep.* **1999**, *18*, 9−16.
(53) Le Poul, N.; Campion, M.; Douziech, B.; Rondelez, Y.; Le Clainche, L.; Reinaud, O.; Le Mest, Y. Monocopper Center Embedded in a Biomimetic Cavity: From Supramolecular Control of Copper Coordination to Redox Regulation. *J. Am. Chem. Soc.* **2007**, *129*, 8801−8810.
(54) Prins, R. Visible absorption spectra of substituted ferricenium cations. *J. Chem. Soc. D* **1970**, 280−281.
(55) Thordarson, P. Determining association constants from titration experiments in supramolecular chemistry. *Chem. Soc. Rev.* **2011**, *40*, 1305−1323.
(56) Clore, G. M.; Iwahara, J. Theory, Practice, and Applications of Paramagnetic Relaxation Enhancement for the Characterization of Transient Low-Population States of Biological Macromolecules and Their Complexes. *Chem. Rev.* **2009**, *109*, 4108−4139.
(57) Osella, D.; Carretta, A.; Nervi, C.; Ravera, M.; Gobetto, R. Inclusion Complexes of Ferrocenes and β-Cyclodextrins. Critical Appraisal of the Electrochemical Evaluation of Formation Constants. *Organometallics* **2000**, *19*, 2791−2797.
(58) Connelly, N. G.; Geiger, W. E. Chemical Redox Agents for Organometallic Chemistry. *Chem. Rev.* **1996**, *96*, 877−910.

DOI: 10.1021/jacs.8b09321
J. Am. Chem. Soc. 2018, 140, 14590−14594

Supplementary Information

A Redox-Switchable, Allosteric Coordination Complex

Ho Fung Cheng,[†] Andrea I. d'Aquino,[†] Joaquín Barroso-Flores,[‡] and Chad A. Mirkin[*,†]

[†]Department of Chemistry and International Institute for Nanotechnology, Northwestern University, 2145 Sheridan Road, Evanston, Illinois 60208-3113, United States

[‡]Centro Conjunto de Investigación en Química Sustentable, UAEM-UNAM, Carretera Toluca-Atlacomulco Km 14.5, Personal de la UNAM, Unidad San Cayetano, Toluca, Estado de México C.P. 50200, Mexico

Table of Contents

General Methods

All chemicals, reagents, and solvents were purchased as reagent grade from Sigma-Aldrich, Acros, or Alfa Aesar and used as received unless otherwise stated. When specified, solvents were degassed under a stream of argon before use. All glassware and stir bars were oven-dried at 180 °C. Flash chromatography was performed using SiO_2 60 (230–400 mesh ASTM, 0.040–0.063 mm; Fluka). Deuterated solvents were purchased from Cambridge Isotope Laboratories and Sigma Aldrich and used as received. ^{1}H, ^{31}P, ^{19}F, and ^{195}Pt NMR spectra were recorded on a Bruker Avance 400 MHz NMR spectrometer at 298 K, and chemical shifts (δ) are given in parts per million. ^{1}H NMR spectra were referenced to residual proton resonances in the deuterated solvents (dichloromethane-d_2 = δ 5.32; nitromethane-d_3 = δ 4.33), while absolute referencing was applied for heteronuclear NMR spectra (Ξ_C = 25.145020; Ξ_P = 40.480742; Ξ_F = 94.094011). High resolution mass spectra (HRMS) were recorded on an Agilent 6120 LC-TOF instrument in positive ion mode. Fe(η^5-C_5H_5)(η^5-$C_5H_4SCH_2CH_2Cl$) was synthesized following literature procedures.[1]

Synthesis

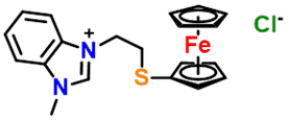

RHL ligand precursor (1). Fe(η^5-C_5H_5)(η^5-$C_5H_4SCH_2CH_2Cl$) (0.626 g, 2.23 mmol) and 1-methylbenzimidazole (0.35 g, 2.68 mmol) were dissolved in 25 mL of anhydrous acetonitrile (MeCN). The bright red reaction mixture, which gradually turned brown, was stirred and refluxed at 100 °C for three days under N_2 atmosphere. The mixture was dried and purified via flash chromatography (CH_2Cl_2:MeOH = 10:1, R_f = 0.11). The product fraction was dried *in vacuo* to obtain a yellow solid (0.1315 g, 0.319 mmol, isolated yield = 14%; unreacted Fe(η^5-C_5H_5)(η^5-$C_5H_4SCH_2CH_2Cl$) was recovered and reused). ^{1}H NMR (400 MHz, CD_2Cl_2) δ 11.80 (s, 1H), 7.70 – 7.57 (m, 3H), 7.55 – 7.48 (m, 1H), 4.66 (t, J = 6.6 Hz, 2H), 4.29 (t, J = 1.8 Hz, 2H), 4.22 (s, 3H), 4.18 (t, J = 1.8 Hz, 2H), 4.17 (s, 5H), 3.24 (t, J = 6.6 Hz, 2H). ^{13}C NMR (101 MHz, CD_2Cl_2) δ 144.29, 131.99, 131.17, 126.88, 126.85, 112.75, 112.64, 77.50, 73.83, 69.57, 69.53, 53.93, 53.66, 53.39, 53.12, 52.85, 50.18, 47.03, 36.38, 33.40. HRMS (ESI+) m/z Calcd for $[M–Cl]^+$: 377.0766 *m/z*.

Found: 377.0770 *m/z*. Single crystals suitable for X-ray diffraction studies were obtained by slow diffusion of diethyl ether (Et_2O) into a 1,2-dichloroethane solution of **1**.

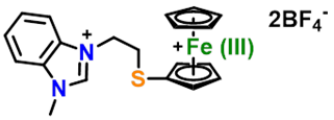

Oxidized RHL ligand precursor ($\mathbf{1^{ox}}$). To a degassed nitromethane-d_3 (CD_3NO_2) solution of **1** (4.8 mg, 0.00116 mmol), $AgBF_4$ (5 mg, 0.0257 mmol) was added in the glovebox. The resulting reddish brown solution was filtered for spectroscopic characterization (by ^{1}H NMR spectroscopy = 100% conversion). ^{1}H NMR (400 MHz, CD_3NO_2) δ 39.36 (s, 2H, br), 35.63 (s, 2H, br), 30.00 (s, 5H, br), 10.94 (s, 1H), 9.51 (d, J = 8.1 Hz, 1H), 9.15 (d, J = 7.7 Hz, 1H), 8.82 (t, J = 7.6 Hz, 1H), 8.72 (d, J = 6.4 Hz, 1H), 5.88 (s, 2H), 5.63 (s, 3H), 5.30 (s, 2H). ^{19}F NMR (376 MHz, CD_3NO_2) δ -153.89, -153.95. Single crystals suitable for X-ray diffraction studies were obtained by layering benzene over a CD_3NO_2 solution of $\mathbf{1^{ox}}$.

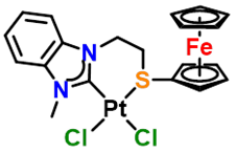

Monoligated complex (2). A solution of **1** (0.1254 g, 0.304 mmol) in dichloromethane (CH_2Cl_2) (3 mL) was combined with Ag_2O (35.2 mg, 0.152 mmol) and stirred at 43 °C. After several minutes, a solution of $PtCl_2$(cod) (0.1137 g, 0.304 mmol) in CH_2Cl_2 (3 mL) was added, and the mixture was shielded from light and stirred overnight. The resulting suspension was filtered and the supernatant was concentrated *in vacuo*, and hexane was added to precipitate a yellow solid. The yellow product was isolated via centrifugation. The precipitates were washed with Et_2O (10 mL x 3) and dried *in vacuo* to afford monoligated complex **2** as a yellow powder (0.1939 g, 0.302 mmol, isolated yield = 99%). ^{1}H NMR (400 MHz, CD_2Cl_2) δ 7.54 (dt, *J* = 7.9, 1.0 Hz, 1H), 7.48 – 7.34 (m, 3H), 4.78 – 4.61 (m, 1H), 4.54 (d, *J* = 14.7 Hz, 1H), 4.48 (d, *J* = 0.7 Hz, 5H), 4.33 (s, 3H), 4.24 (s, 1H), 4.15 (d, *J* = 2.6 Hz, 2H), 3.82 – 3.72 (m, 1H), 3.63 (d, *J* = 13.6 Hz, 1H), 2.37 (td, *J* = 13.0, 4.0 Hz, 1H). ^{13}C NMR (101 MHz, CD_2Cl_2) δ 134.73, 132.36, 124.24, 124.19, 111.23, 109.91, 80.20, 70.72, 70.08, 69.90, 69.68, 53.93, 53.66, 53.39, 53.12, 52.85, 46.08, 40.98, 34.64, 30.83. ^{195}Pt NMR (86 MHz, CD_2Cl_2) δ -3598.48. HRMS (ESI+) m/z Calcd for $[M–Cl]^+$: 607.0020 *m/z*. Found: 607.0029 *m/z*. Single crystals suitable for X-ray

diffraction studies were obtained by slow diffusion of Et_2O into a 1,2-dichloroethane solution of **2**.

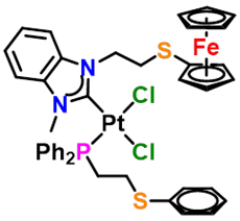

Fully open complex (3). Monoligated complex (**2**) (58.4 mg, 0.0909 mmol) and (2-(phenylthio)ethyl)diphenylphosphine (29.4 mg, 0.0909 mmol) were combined in CH_2Cl_2 and stirred at room temperature for 3 h. The solution was concentrated *in vacuo* and the product was purified via slow diffusion of Et_2O into a solution of **3** in CH_2Cl_2 to form a yellow precipitate. The precipitate was dried *in vacuo* to afford fully open complex **3** as a yellow powder (84.9 mg, 0.0880 mmol, isolated yield = 97%; after purification: 82.7 mg, 0.0857 mmol, isolated yield = 94%). ^{1}H NMR (400 MHz, CD_2Cl_2) δ 7.47 – 6.70 (m, 19H), 4.70 – 4.56 (m, 1H), 4.56 – 4.11 (m, 9H), 3.78 (s, 3H), 3.74 – 3.63 (m, 1H), 3.40 – 3.21 (m, 3H), 2.98 (dddd, J = 25.9, 15.9, 9.7, 5.6 Hz, 2H), 2.69 – 2.58 (m, 1H). ^{31}P NMR (162 MHz, CD_2Cl_2) δ 1.30 (s, $J_{P–Pt}$ = 3765 Hz). ^{195}Pt NMR (86 MHz, CD_2Cl_2) δ -3994.57, -4038.71. HRMS (ESI+) m/z Calcd for $[M–Cl]^+$: 929.0972 *m/z*. Found: 929.0966 *m/z*.

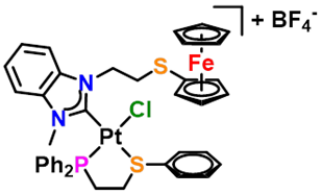

Semi-open complex (4). To an acetone solution of **3** (80.1 mg, 0.0830 mmol), $AgBF_4$ (16.2 mg, 0.0830 mmol) was added. The mixture was shielded from light and allowed to stir overnight at room temperature. The resulting suspension was filtered, and the supernatant was dried *in vacuo* to afford pure semi-open complex **4** as a yellow solid (79.1 mg, 0.0779 mmol, isolated yield = 94%). ^{1}H NMR (400 MHz, CD_2Cl_2) δ 8.05 – 6.93 (m, 19H), 4.83 – 3.88 (m, 10H), 3.75 (d, J = 7.6 Hz, 3H), 3.57 (s, 1H), 3.40 – 3.22 (m, 1H), 3.22 – 2.70 (m, 4H), 2.59 (s, 1H). ^{31}P NMR (162 MHz, CD_2Cl_2) δ 37.02 (s, $J_{P–Pt}$ = 3417 Hz). HRMS (ESI+). Calcd for $[M–BF_4]^+$: 929.0972 *m/z*. Found: 929.0974 *m/z*.

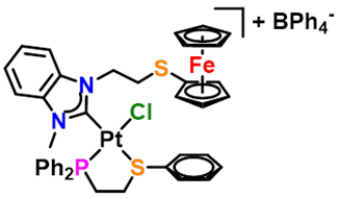

Semi-open complex (4), counteranion BPh_4^-. To a methanol (MeOH) solution of **3** (7.7 mg, 0.00798 mmol), excess $NaBPh_4$ (3.4 mg, 0.00994 mmol) was added and a pale yellow precipitate appeared. The resulting suspension was filtered, and the collected precipitate was washed with cold MeOH and dried *in vacuo* to afford semi-open complex **4** as a yellow solid (8.2 mg, 0.00657 mmol, isolated yield = 82%), which can be purified via crystallization (see below for procedure). ^{1}H NMR (400 MHz, CD_2Cl_2) δ 7.93 – 7.30 (m, 19H), 7.28 – 6.79 (m, 23H), 4.58 – 4.19 (m, 9H), 4.19 – 2.08 (m, 11H). ^{31}P NMR (162 MHz, CD_2Cl_2) δ 36.77 (s, $J_{P–Pt}$ = 3410 Hz). Single crystals suitable for X-ray diffraction studies were obtained by slow diffusion of Et_2O into a CH_2Cl_2 solution of **4**.

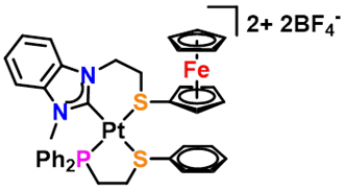

Fully closed complex (5). To an acetone solution of **4** (68.1 mg, 0.0670 mmol), $AgBF_4$ (13 mg, 0.0670 mmol) was added. The mixture was shielded from light and stirred overnight at room temperature. The resulting suspension was filtered, and the supernatant was dried *in vacuo* to afford fully closed complex **5** as an orange-yellow solid (68.3 mg, 0.0640 mmol, isolated yield = 95%). The product can be purified via crystallization (see below for procedure, 95% recovery). ^{1}H NMR (400 MHz, CD_2Cl_2) δ 7.99 – 7.26 (m, 19H), 5.12 (d, J = 70.2 Hz, 2H), 4.88 – 3.78 (m, 9H), 3.38 (d, J = 297.3 Hz, 9H). ^{31}P NMR (162 MHz, CD_2Cl_2) δ 42.02 (s, $J_{P–Pt}$ = 3250 Hz), δ 37.24 (s, $J_{P–Pt}$ ~ 3140 Hz). ^{19}F NMR (376 MHz, CD_2Cl_2) δ -150.85, δ -150.90. ^{1}H NMR (400 MHz, CD_3NO_2) δ 8.08 – 7.43 (m, 20H), 5.43 – 4.76 (m, 2H), 4.29 – 3.59 (m, 9H), 3.56 – 2.44 (m, 9H). ^{31}P NMR (162 MHz, CD_3NO_2) δ 41.62 (s, $J_{P–Pt}$ = 3183 Hz), 37.50 (s, $J_{P–Pt}$ ~ 3180 Hz). ^{19}F NMR (376 MHz, CD_3NO_2) δ -152.72, -152.77. HRMS (ESI+). Calcd for $[M–BF_4]^+$: 980.1326 *m/z*. Found: 980.1337 *m/z*. Single crystals suitable for X-ray diffraction studies were obtained by slow diffusion of Et_2O into a CH_2Cl_2 solution of **5**.

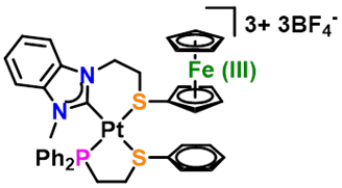

Oxidized, fully closed complex (6). To a degassed CH_2Cl_2 solution of **5** (35.4 mg, 0.0332 mmol), $AgBF_4$ (8mg, 0.0411 mmol) was added in the glovebox. The mixture was shielded from light and allowed to stir overnight at room temperature. The orange solution turned green, which decolorized gradually and formed a dark green precipitate. The resulting suspension was filtered and the filtrate was discarded. The dark green precipitate was dissolved in CD_3NO_2 for spectroscopic characterization (by ^{31}P NMR spectroscopy = 100% conversion). ^{1}H NMR (400 MHz, CD_3NO_2) δ 38.56 (br), 9.74 (br), 8.09, 8.02, 8.01. ^{31}P NMR (162 MHz, CD_3NO_2) δ 39.04 (br), δ -8.08 (br). ^{19}F NMR (376 MHz, CD_3NO_2) δ -154.53, -154.58. HRMS (ESI+). Calcd for $[M–2BF_4+Cl]^+$: 1016.1006 *m/z*. Found: 1016.0987 *m/z*.

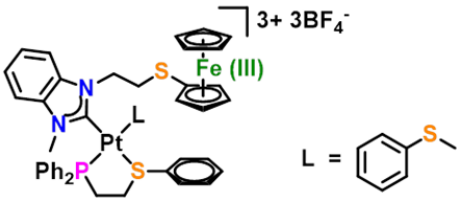

Oxidized, semi-open complex (7). To a degassed CD_3NO_2 solution of **6** (0.0180 mmol) in the glovebox, degassed PhSMe (0.0902 mmol, 10.6 μL) was added to give a reddish brown solution with complex **7** (by ^{31}P NMR spectroscopy = 100% conversion). ^{1}H NMR (400 MHz, CD_3NO_2) δ 39.61 (br), 35.57 (br), 30.04 (br), 14.30 (br), 12.58 (br), 8.11 (br), 7.88 (br), 7.77 (br), 7.48 (br), 7.31 (br), 7.20 (br), 6.19 (br), 4.08 (br), 3.69 (br), 3.36 (br). ^{31}P NMR (162 MHz, CD_3NO_2) δ 41.41 (s, $J_{P–Pt}$ = 2994 Hz). ^{19}F NMR (376 MHz, CD_3NO_2) δ -154.11, -154.17.

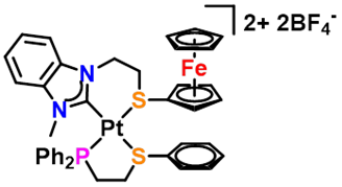

Regeneration of fully closed complex (5). To a degassed CD_3NO_2 solution of **7** (0.0107mmol) in the glovebox, $Fe(Cp^*)_2$ (0.0129 mmol, 4.2 mg) was added to give complex **5** (by ^{31}P NMR spectroscopy = 100% conversion). ^{1}H NMR (400 MHz, complex

5, CD_3NO_2) δ 7.92, 7.86, 7.84, 7.80, 7.79, 7.78, 7.77, 7.74, 7.73, 7.67, 7.62, 7.60, 7.59, 7.58, 7.56, 7.54, 7.53, 7.48, 7.46, 5.33, 5.30, 4.92, 4.22, 4.16, 4.09, 3.75, 3.33, 3.23, 3.02. ^{1}H NMR (400 MHz, PhSMe, CD_3NO_2) δ 7.43 – 7.31 (m, 4H), 7.22 (dd, J = 7.9, 6.1 Hz, 1H), 2.53 (s, 3H). ^{1}H NMR (400 MHz, $Fe(Cp^*)_2$, CD_3NO_2) δ -30.83 (s, 1H). ^{31}P NMR (162 MHz, CD_3NO_2) δ 41.62 (s, $J_{P–Pt}$ = 3188 Hz), 37.62 (s, $J_{P–Pt}$ ~ 3210 Hz). ^{19}F NMR (376 MHz, CD_3NO_2) δ -152.81, -152.86.

Variable-Temperature NMR Studies

Fully closed complex **5** was dissolved in CD_3NO_2 for variable-temperature (VT) NMR experiments. ^{1}H and ^{31}P NMR spectra were taken at increasing temperatures from 298 K to 343 K in 15 K increments.

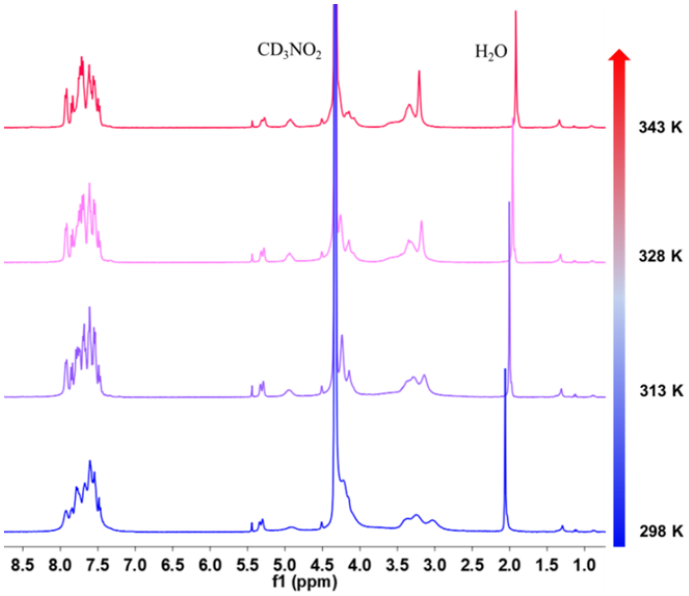

Figure S1. VT ^{1}H NMR (400 MHz, CD_3NO_2) spectra of **5**.

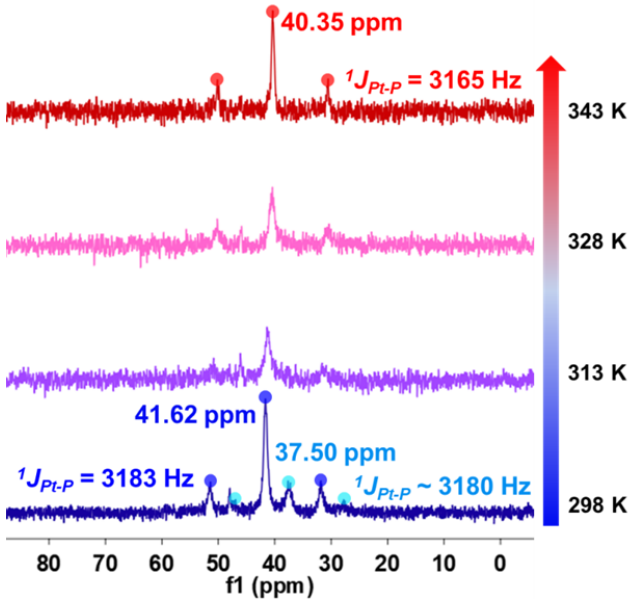

Figure S2. VT ^{31}P NMR (162 MHz, CD_3NO_2) spectra of **5**.

NMR Titrations

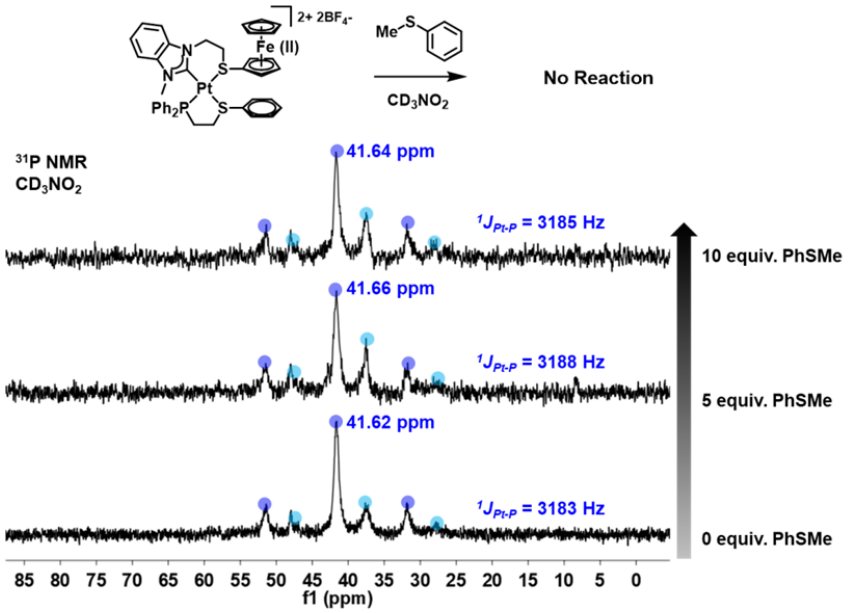

Figure S3. ^{31}P NMR (162 MHz, CD_3NO_2, 298 K) spectra of fully closed complex **5** titrated with increasing equivalents of PhSMe.

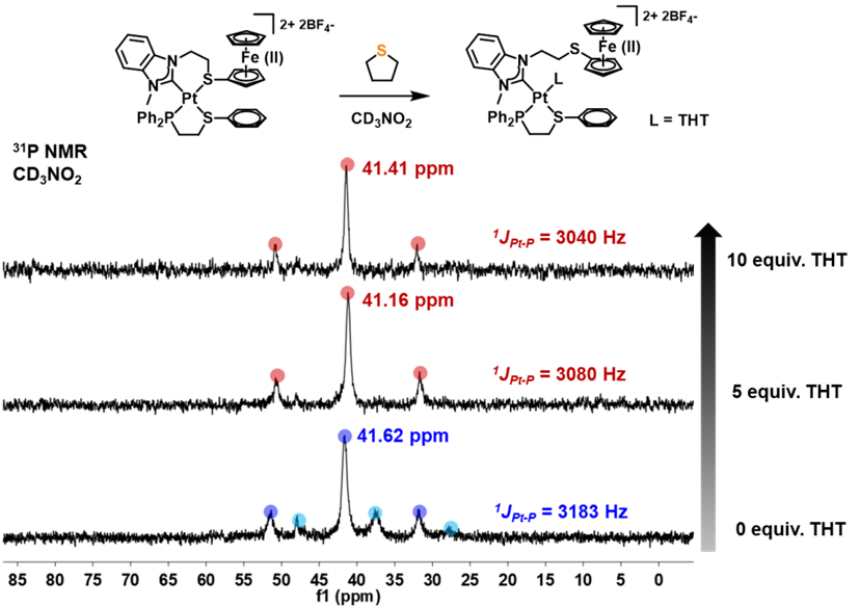

Figure S4. ^{31}P NMR (162 MHz, CD_3NO_2, 298 K) spectra of **5** titrated with increasing equivalents of tetrahydrothiophene (THT). A smaller coupling constant ($^{1}J_{Pt\text{-}P}$ ~ 3030Hz) and the disappearance of the diastereomeric signal at ~ 38 ppm indicate the formation of the semi-open complex.

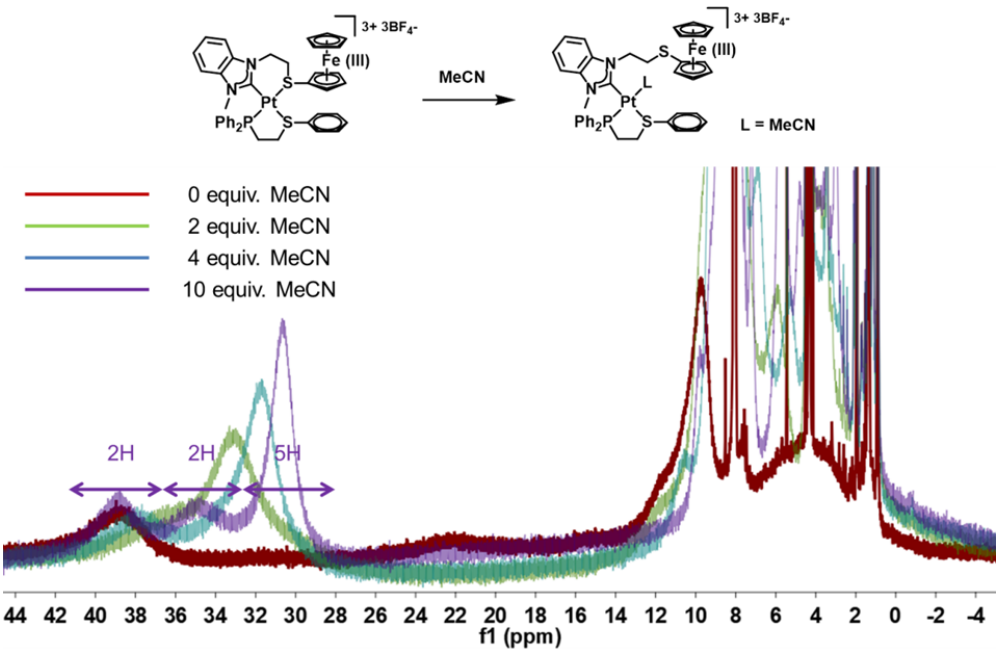

Figure S5. ^{1}H NMR (400 MHz, CD_3NO_2, 298 K) spectra of complex **6** titrated with increasing equivalents of the surrogate ligand, MeCN.

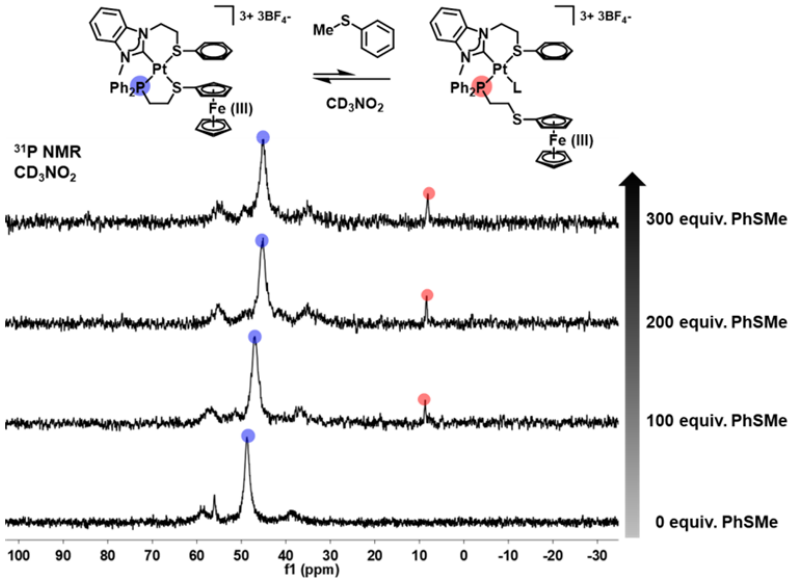

Figure S6. ^{31}P NMR (162 MHz, CD_3NO_2, 298 K) spectra of the oxidized complex titrated with increasing equivalents of PhSMe. The peak at ~8ppm is indicative of a ^{31}P nucleus that is not part of a 5-member chelate.[2] This complex has its redox-active Fc covalently attached to the thioether of the P,S ligand instead of the NHC,S ligand.

One-pot redox regulation

$[N(C_6H_4Br\text{-}4)_3]^+BF_4^-$ was prepared in situ via addition of $AgBF_4$ into a degassed CH_2Cl_2 solution of $N(C_6H_4Br\text{-}4)_3$. The resulting deep blue solution was added to a yellow solution of **5** to give a brown solution of **7**.

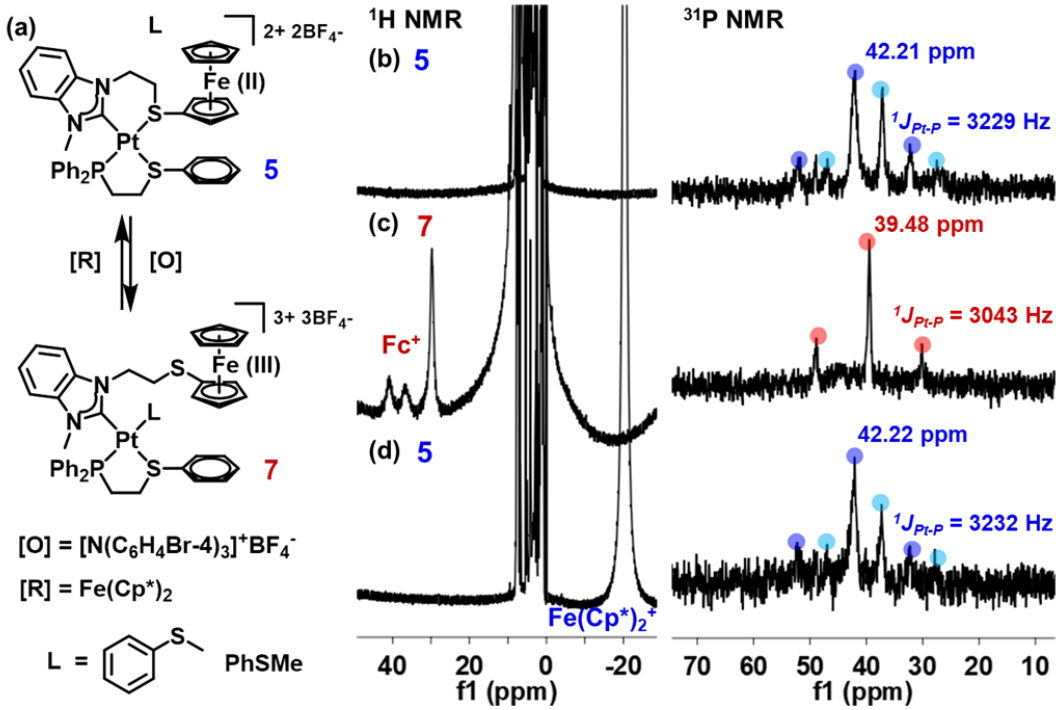

Figure S7. (a) Direct interconversion between complexes **5** and **7**. ^{1}H NMR (400 MHz, CD_2Cl_2, 298 K) and ^{31}P NMR (162 MHz, CD_2Cl_2, 298 K) spectra of (b) **5** with 4.5 equiv of PhSMe, (c) after oxidation by $[N(C_6H_4Br\text{-}4)_3]^+BF_4^-$, and (d) after subsequent reduction by $Fe(Cp^*)_2$.

Alternative surrogate ligands

All transformations were performed, as described in the synthesis section, by substituting PhSMe with a different surrogate ligand in the specified amount. Upon addition of the surrogate ligand, the deep green solution changed into a reddish brown solution.

For the transformation using MeCN as a surrogate ligand, the formation of **7-MeCN** was confirmed spectroscopically (Figure S8d)—a large upfield shift of the ^{31}P resonance (32.69 ppm) and a large coupling constant ($^{1}J_{Pt\text{-}P}$ = 3609 Hz), the latter of which is indicative of a ^{31}P nucleus *trans* to a weakly donating ligand such as MeCN. The gradual opening of **6** by MeCN was also followed by ^{1}H NMR via titrating increasing equivalents of MeCN (Figure S5).

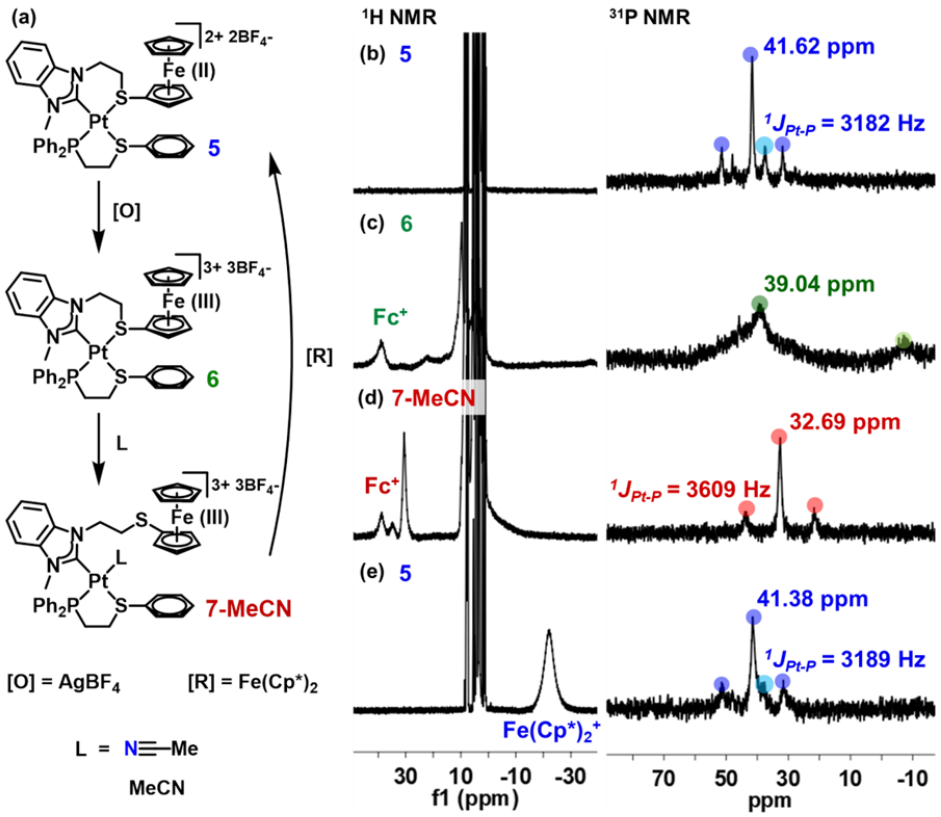

Figure S8. (a) Interconversion of **5**, **6**, and **7-MeCN**. ^{1}H NMR (400 MHz, CD_3NO_2, 298 K) and ^{31}P NMR (162 MHz, CD_3NO_2, 298 K) spectra of (b) **5**, after sequential addition of (c) $AgBF_4$, (d) 10 equiv of MeCN, and (e) $Fe(Cp^*)_2$.

For the transformation using tetrahydrothiophene (THT) as a surrogate ligand, the formation of **7-THT** was marked by the disappearance of diastereomeric signal (Figure S9d) and a decrease in coupling constant ($^{1}J_{Pt\text{-}P}$ = 2948 Hz). Note that upon reduction of **7-THT** by $Fe(Cp^*)_2$, instead of re-forming **5** directly, the non-oxidized, semi-open complex **8-THT** was formed. This is consistent with the titration experiment that shows that THT is a strongly coordinating ligand for **5** (Figure S4).

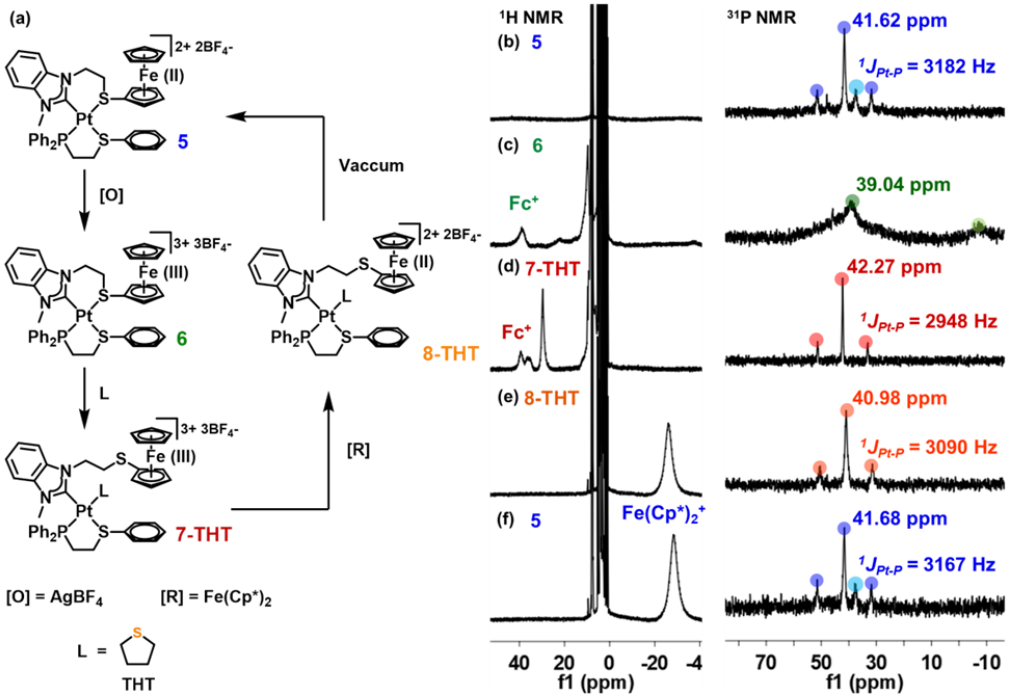

Figure S9. (a) Interconversion of **5**, **6**, **7-THT**, and **8-THT**. ^{1}H NMR (400 MHz, CD_3NO_2, 298 K) and ^{31}P NMR (162 MHz, CD_3NO_2, 298 K) spectra of (b) **5**, after addition of (c) $AgBF_4$, (d) 5 equiv of THT, and (e) $Fe(Cp^*)_2$. (f) *In vacuo* overnight.

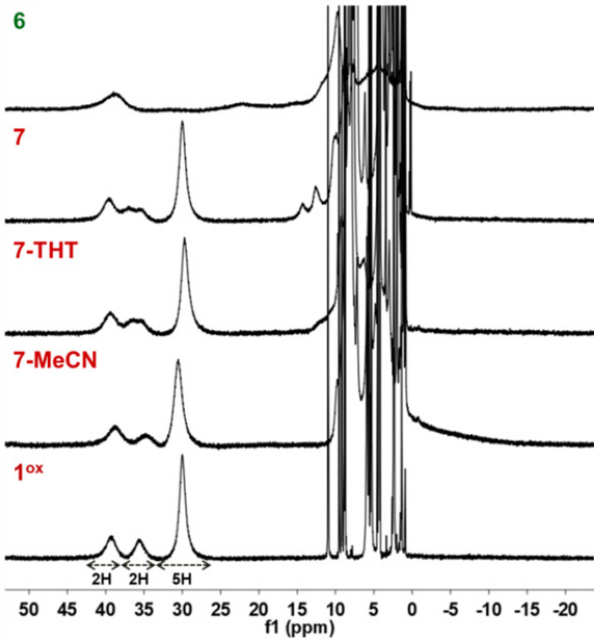

Figure S10. ^{1}H NMR (400 MHz, CD_3NO_2, 298 K) spectra of oxidized complexes (fully closed **6**, semi-open **7**, **7-THT**, and **7-MeCN**), and oxidized RHL ligand precursor (**1**^{ox}).

^{1}H DOSY NMR Experiments

A series of ^{1}H DOSY NMR experiments were performed to further confirm that the surrogate ligand PhSMe opens only the oxidized complex **6** but not complex **5**. If the surrogate ligands were to interact with WLA complexes, they would co-diffuse and result in a lower diffusion coefficient for PhSMe. As shown in Table S1, the calculated diffusion coefficient of PhSMe exhibited negligible changes without **5** (1.85 x 10^{-9} m^2s^{-1}) or with **5** (1.86 x 10^{-9} m^2s^{-1}) in the solution. This is highly consistent with the fact that PhSMe does not open **5**. On the other hand, the diffusion coefficient of PhSMe decreased drastically when the oxidized, semi-open complex **7** is present in the solution (1.61 x 10^{-9} m^2s^{-1}), suggesting that PhSMe interacts with the oxidized complex. Reduction with $Fe(Cp^*)_2$ led to an increase in the diffusion coefficient of PhSMe (2.00 x 10^{-9} m^2s^{-1}), consistent with PhSMe decoordination upon reduction of the RHL.

Table S1. Diffusion coefficients (unit: $10^{-9}m^2s^{-1}$) determined by ^{1}H DOSY NMR experiments (400 MHz, CD_3NO_2, 298 K).

Sample	CD_3NO_2 (Solvent)	PhSMe
Only PhSMe	2.50	1.85
5 + 10 equiv of PhSMe	2.46	1.86
7 + 5 equiv of PhSMe	2.56	1.61
7 + 5 equiv of PhSMe, then $Fe(Cp^*)_2$	2.62	2.00

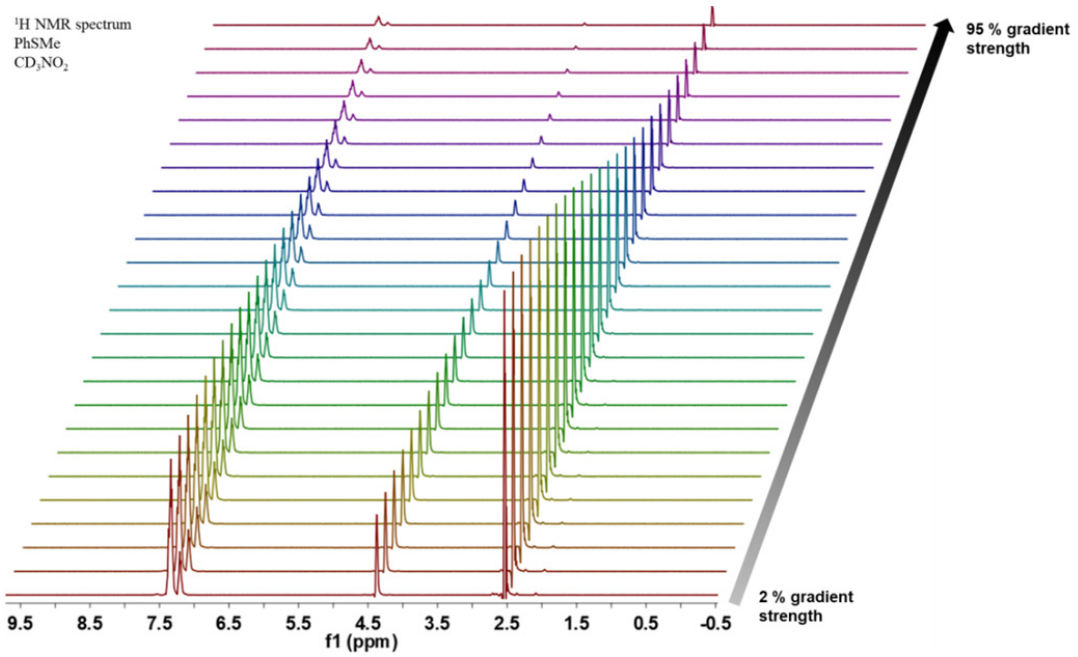

Figure S11. ^{1}H NMR (400 MHz, CD_3NO_2, 298 K) spectra of PhSMe.

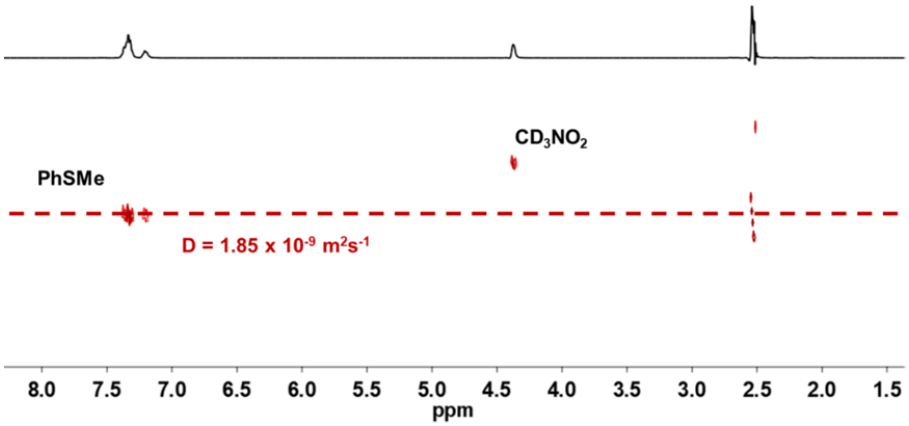

Figure S12. ^{1}H DOSY NMR (400 MHz, CD_3NO_2, 298 K) spectrum of PhSMe.

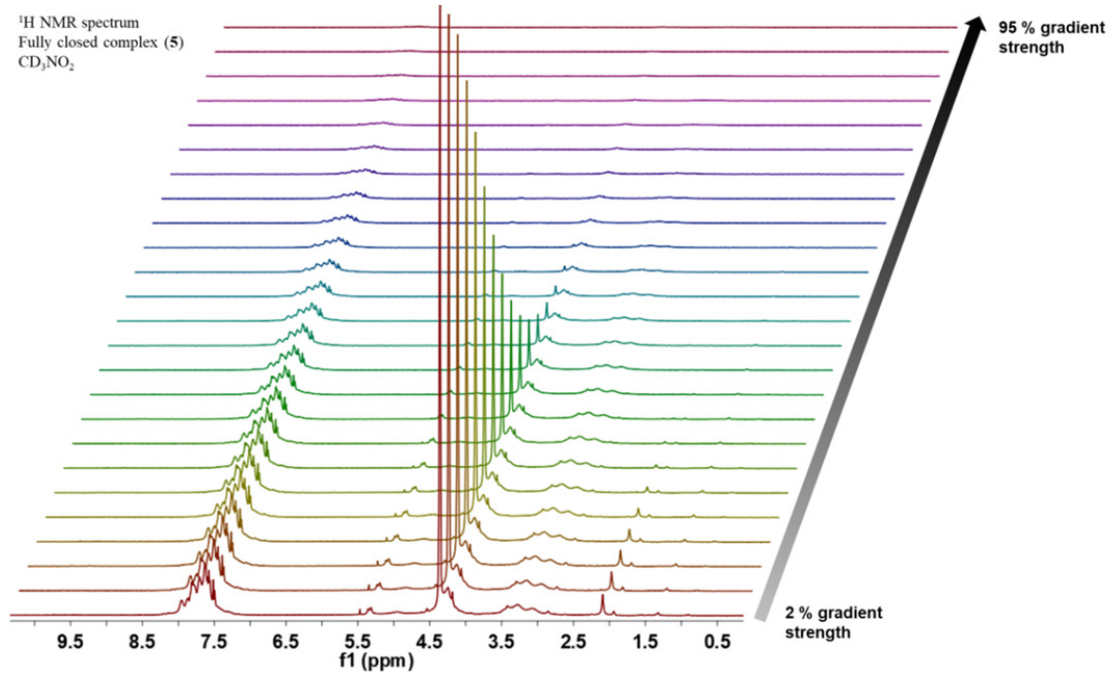

Figure S13. ^{1}H NMR (400 MHz, CD_3NO_2, 298 K) spectra of **5**.

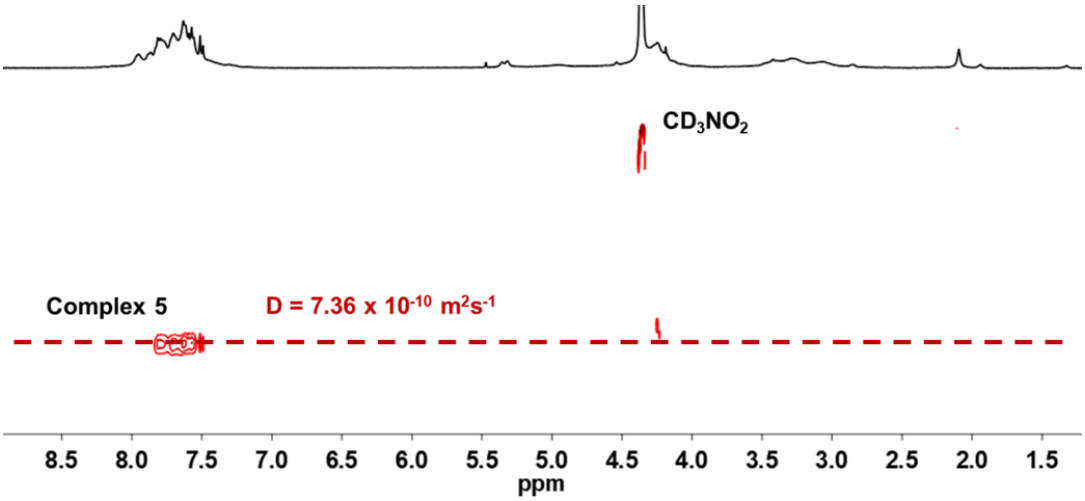

Figure S14. ^{1}H DOSY NMR (400 MHz, CD_3NO_2, 298 K) spectrum of **5**.

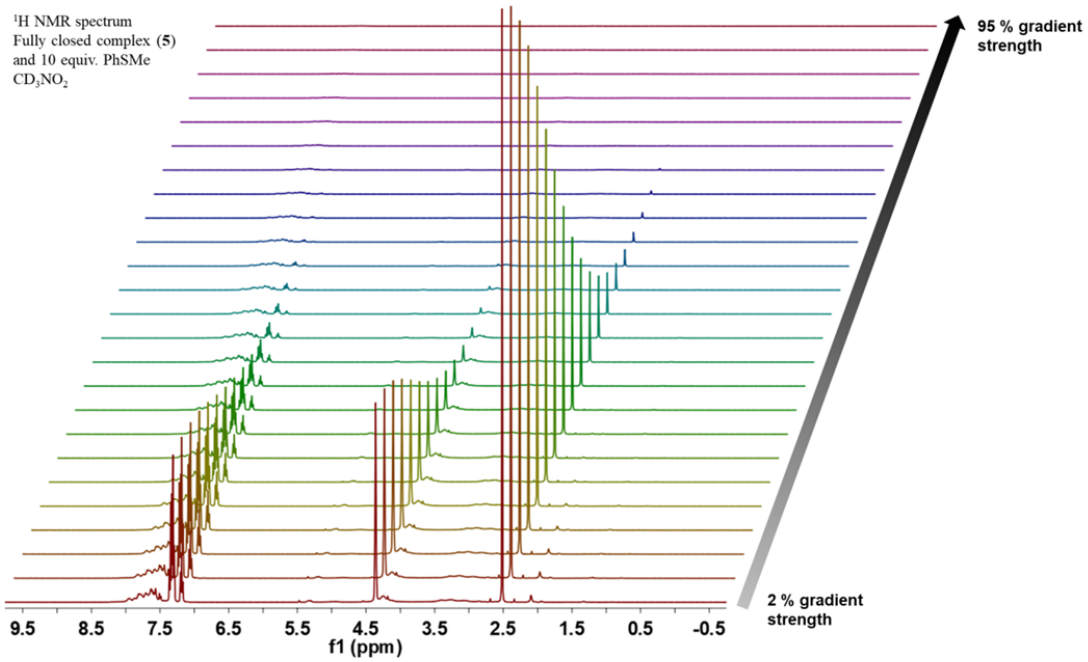

Figure S15. ^{1}H NMR (400 MHz, CD_3NO_2, 298 K) spectra of **5** and 10 equiv of PhSMe.

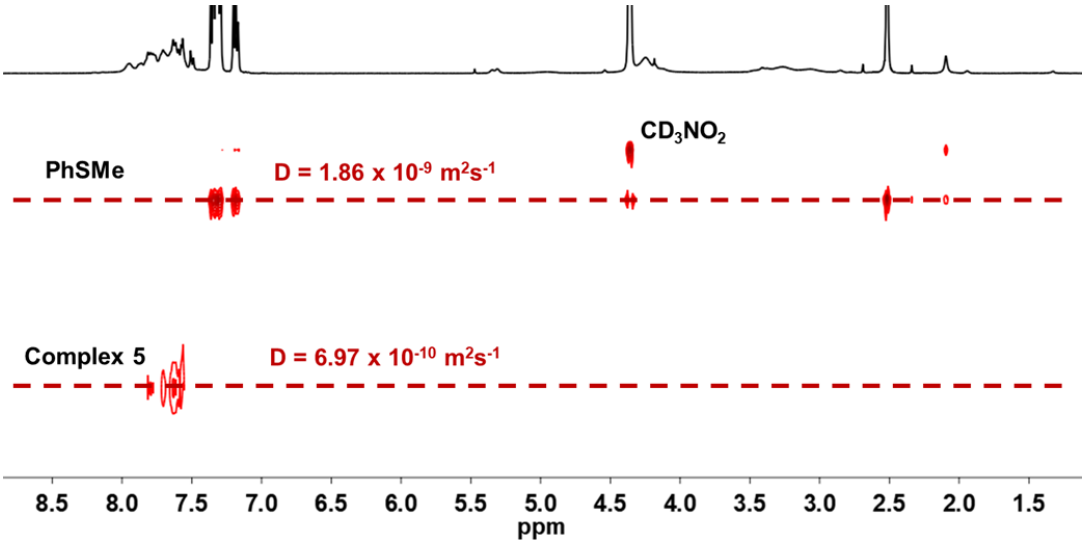

Figure S16. ^{1}H DOSY NMR (400 MHz, CD_3NO_2, 298 K) spectrum of **5** and 10 equiv of PhSMe.

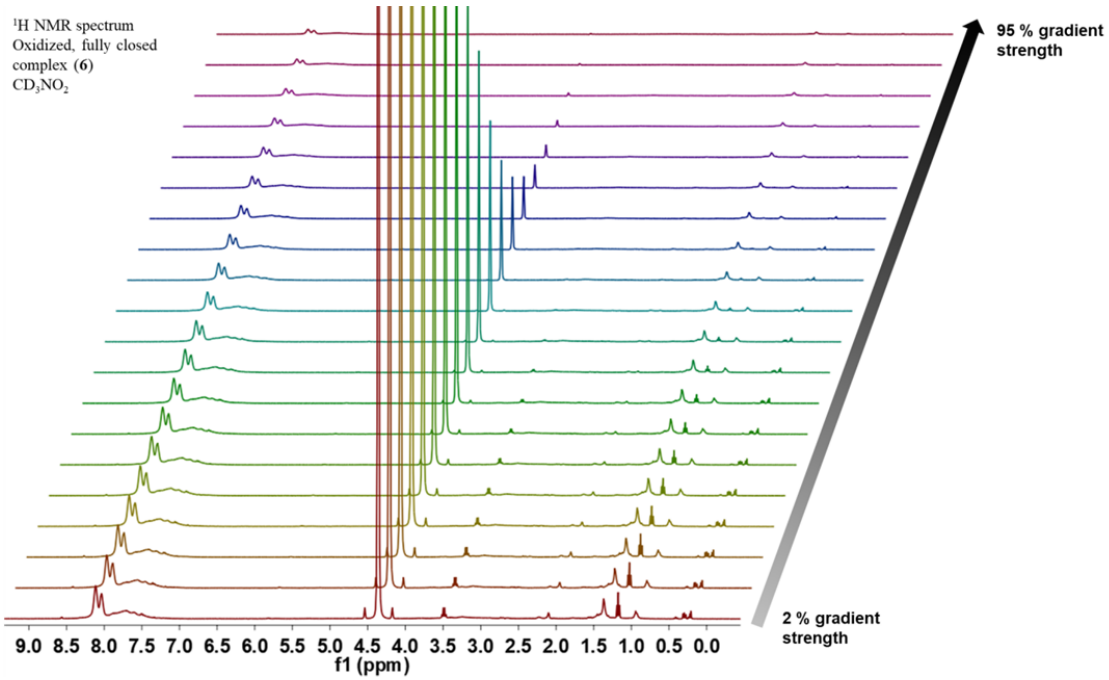

Figure S17. ^{1}H NMR (400 MHz, CD_3NO_2, 298 K) spectra of **6**.

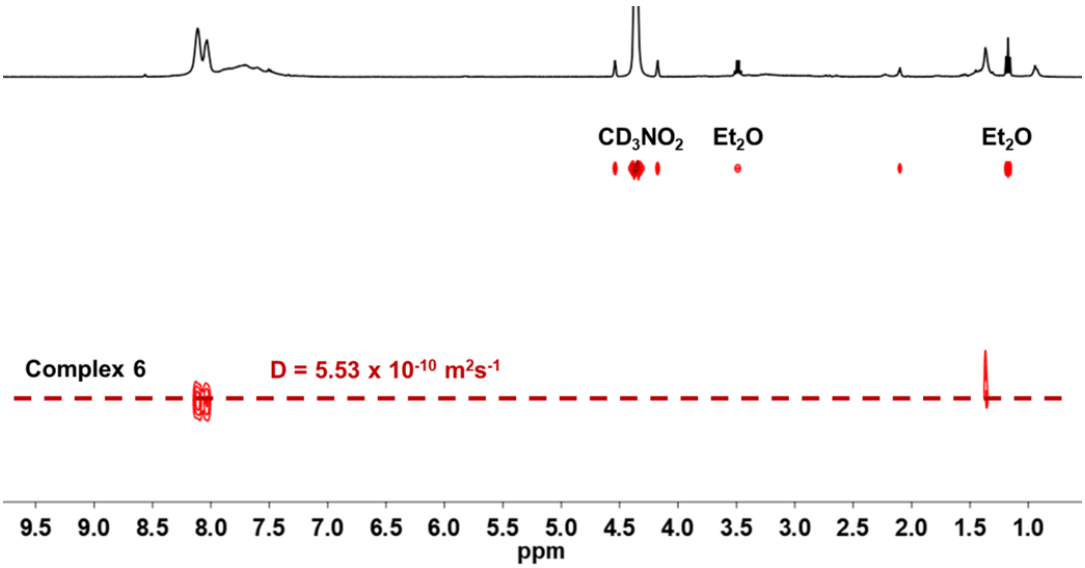

Figure S18. ^{1}H DOSY NMR (400 MHz, CD_3NO_2, 298 K) spectrum of **6**.

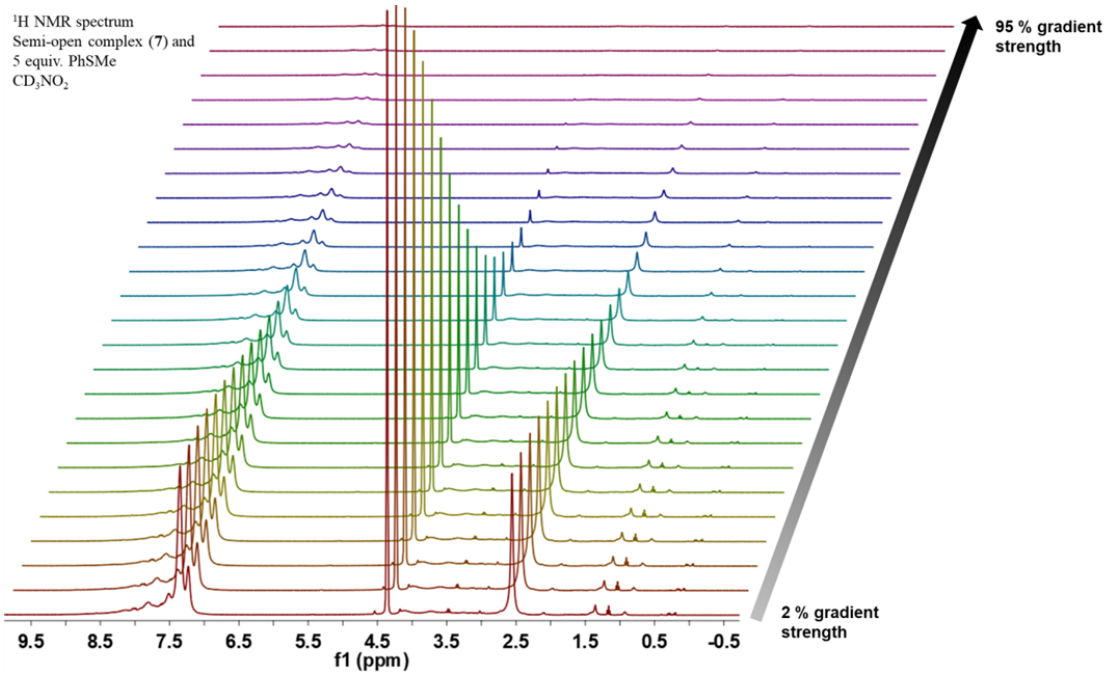

Figure S19. ^{1}H NMR (400 MHz, CD_3NO_2, 298 K) spectra of **7** and 5 equiv of PhSMe.

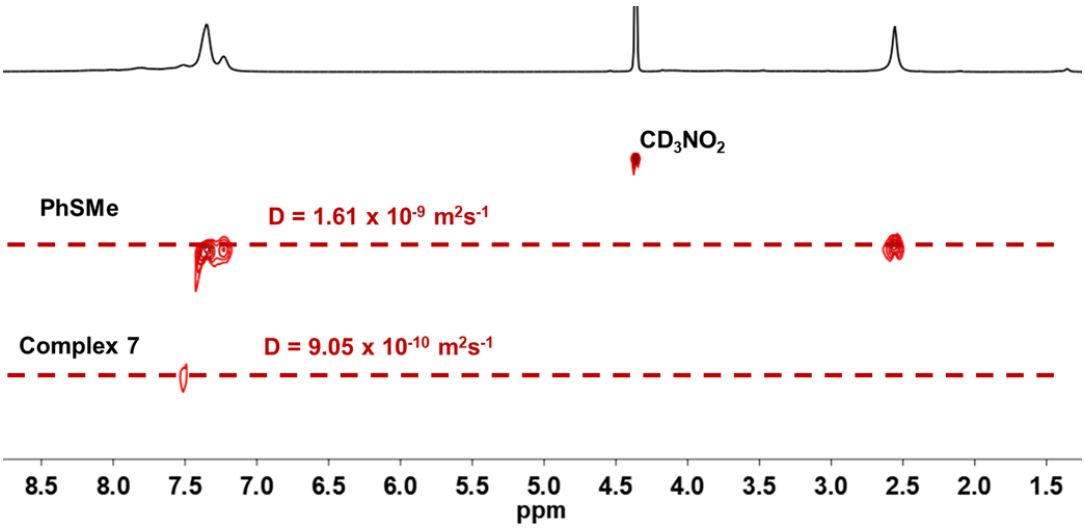

Figure S20. ^{1}H DOSY NMR (400 MHz, CD_3NO_2, 298 K) spectrum of **7** and 5 equiv of PhSMe.

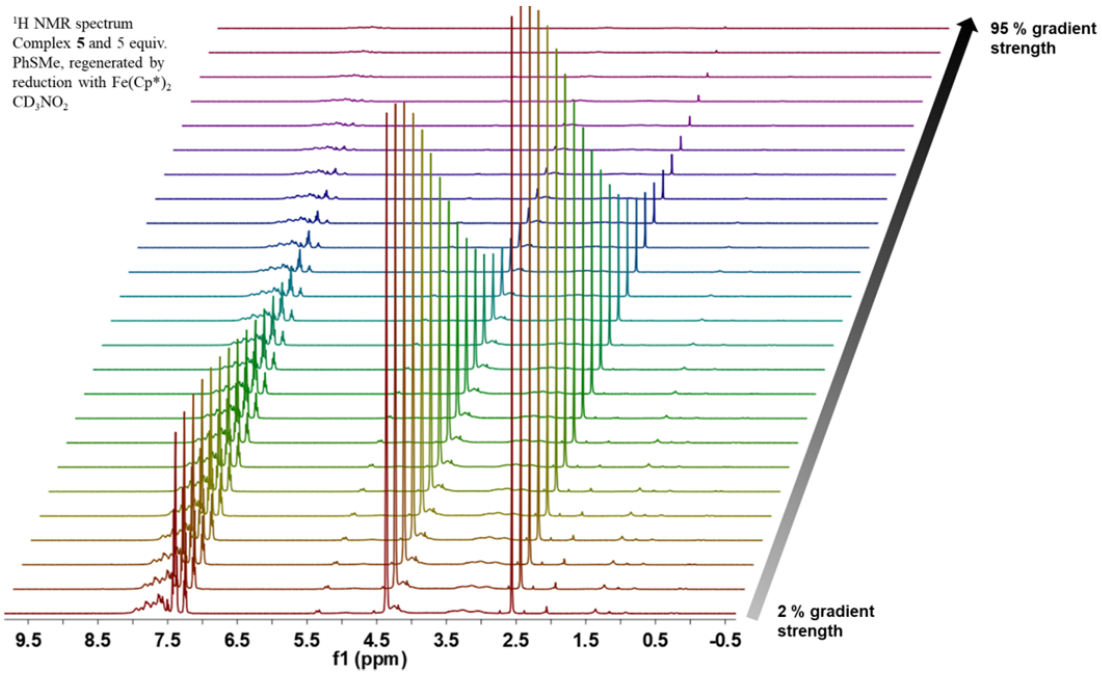

Figure S21. ^{1}H NMR (400 MHz, CD_3NO_2, 298 K) spectra of 5 equiv of PhSMe and **5**, regenerated by reduction of the oxidized complex **7** with Fe(Cp*)$_2$.

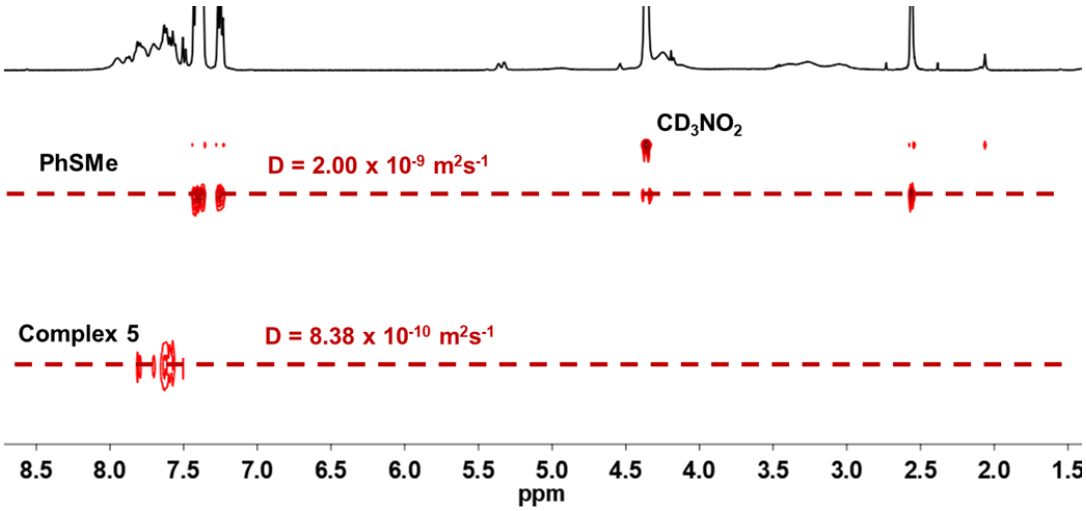

Figure S22. ^{1}H DOSY NMR (400 MHz, CD_3NO_2, 298 K) spectrum of 5 equiv of PhSMe and **5**, regenerated by reduction of the oxidized complex **7** with Fe(Cp*)$_2$.

Electrochemical Studies

Cyclic voltammograms were recorded in a 10 mL scintillation vial with electrodes fixed in position. The analyte was dissolved as a 1.0 mM solution in CH_2Cl_2 (5 mL) with 0.1 M $[nBu_4N][PF_6]$ as the supporting electrolyte. All experiments were performed with a glassy-carbon working electrode (3.0 mm diameter), a coiled platinum-wire counter electrode (23 cm, 0.5 mm diameter), and a non-aqueous Ag/Ag^+ pseudo-reference electrode, which were purchased from BASi. The working electrode was polished with 15 µm and then 1 µm diamond paste and was rinsed with water, MeOH, and CH_2Cl_2 prior to use. Decamethylferrocene (E = 0.548 V vs Fc/Fc^+ in 0.1 M $[nBu_4N][PF_6]/CH_2Cl_2$) was added at the end of the experiments and used as an internal reference,[3] and all potentials were reported referenced to Fc/Fc^+.

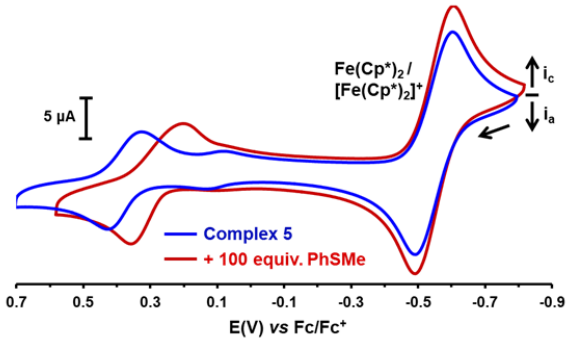

Figure S23. Cyclic voltammograms recorded in 0.1 M $[nBu_4N][PF_6]/CH_2Cl_2$ with $Fe(Cp^*)_2$ added as an internal reference.

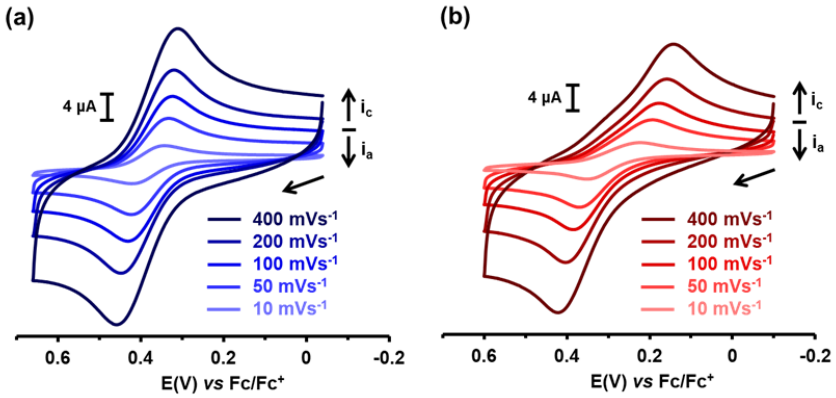

Figure S24. Cyclic voltammograms of (a) **5** and (b) **5** with 100 equiv of PhSMe recorded in 0.1 M $[nBu_4N][PF_6]/CH_2Cl_2$ at varying scan rates.

Ultraviolet-visible-near infrared spectra

Ultraviolet-visible-near infrared (UV-Vis-NIR) spectra were obtained with a Cary 5000 UV-Vis-NIR spectrometer and a 10 mm path length screw-capped quartz cell. Samples were prepared in the glovebox. Each binding isotherm was fitted to a 1:1 binding model to obtain an association constant via non-linear regression.[4] The association constant (K_a) was taken as the average of the values obtained from two different titrations.

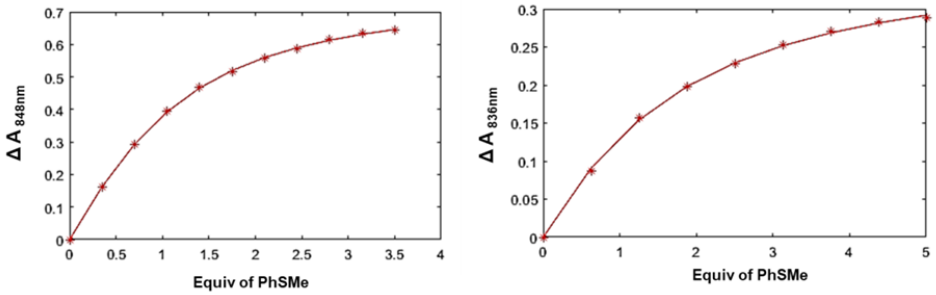

Figure S25. Binding isotherms of **6** and PhSMe in nitromethane. Initial concentration of **6**: 1.01 mM (left) and 0.442 mM (right).

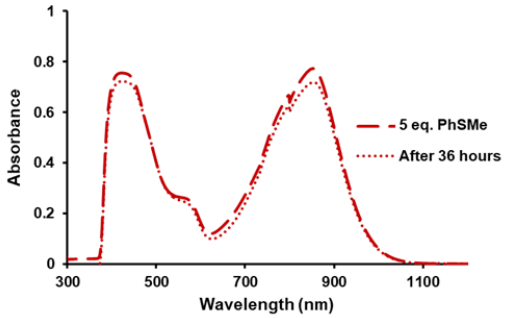

Figure S26. UV-Vis-NIR spectrum of **7** in nitromethane over 36 h.

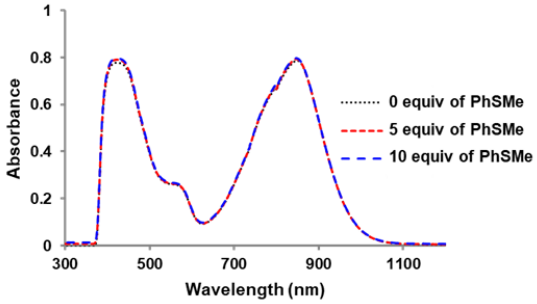

Figure S27. UV-Vis-NIR spectrum of $\mathbf{1}^{ox}$ in nitromethane. Titration experiments show that PhSMe does not interact with the S-Fc^+ moiety.

Crystallographic Information

Suitable single crystals of **1**, **1^{ox}**, **2**, **4**, and **5** were selected and mounted on a MITIGEN holder in Paratone oil on a Bruker Kappa APEX-II CCD diffractometer. All measurements were made with graphite-monochromated Mo Kα radiation. Using Olex2,[5] the structure was solved with the ShelXT structure solution program,[6] using Intrinsic Phasing (for **1**, **1^{ox}**, **2**, and **5**) or Dual Space (for **4**) and refined with the ShelXL refinement package using Least Squares minimization.[7]

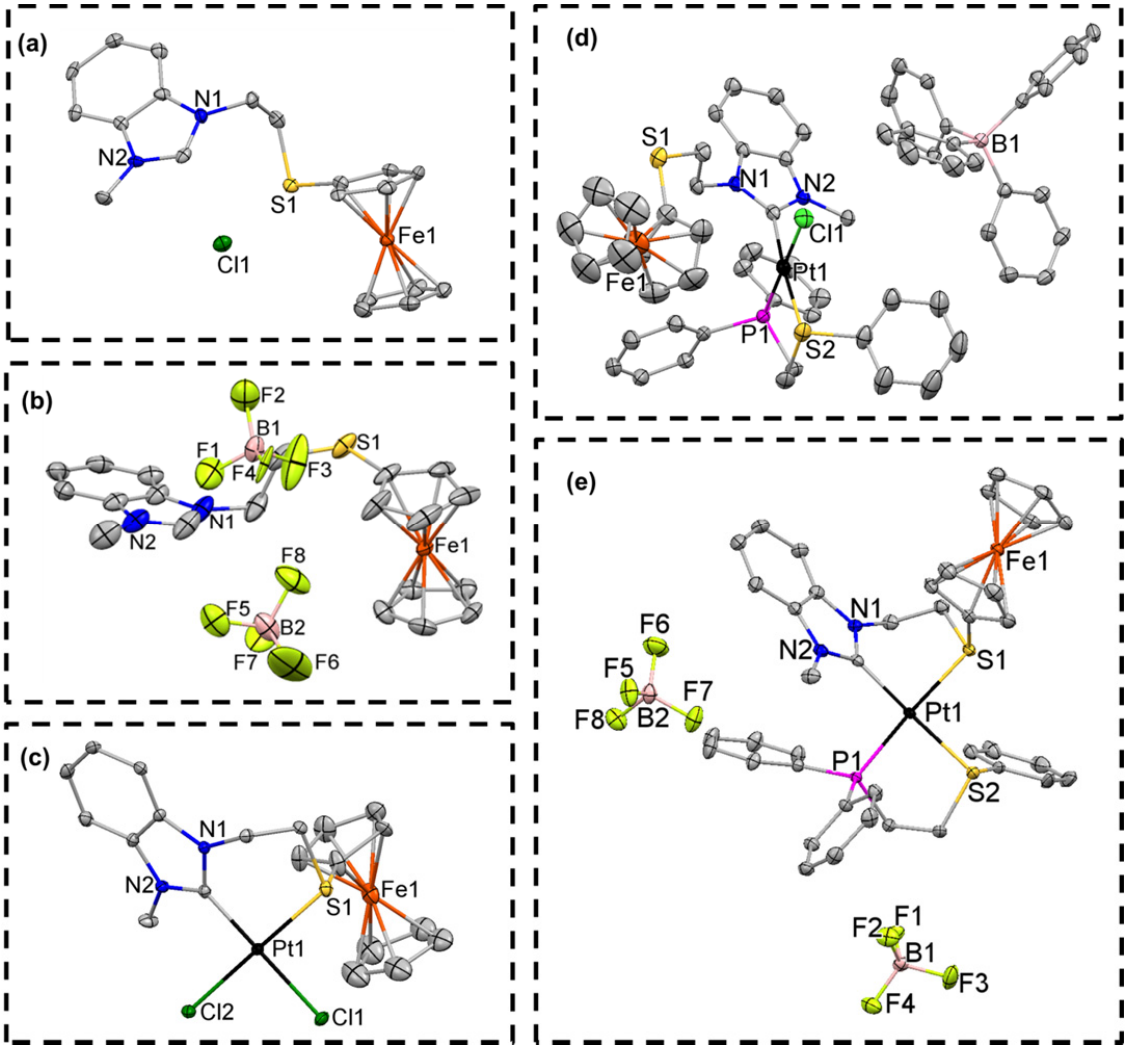

Figure S28. Crystal structures of (a) **1**, (b) **1^{ox}**, (c) **2**, (d) **4**, and (e) **5** drawn with 50% probability thermal ellipsoids. Solvent molecules and H atoms are omitted for clarity.

Table S2. Crystallographic Data for **1**, $\mathbf{1^{ox}}$ and **2**.

	1	$\mathbf{1^{ox}}$	**2**
Empirical formula	$C_{20}H_{22}ClFeN_2O_{0.5}S$	$C_{20}H_{21}B_2N_2F_8SFe$	$C_{22}H_{24}Cl_4FeN_2PtS$
Formula weight	421.75	550.92	741.23
Temperature / K	100.09	100.0	99.94
Crystal system	monoclinic	monoclinic	monoclinic
Space group	$P2_1/c$	$P2_1/n$	$P2_1/c$
a / Å, b / Å, c / Å	17.6572(8), 11.1718(4), 9.4143(6)	11.8881(4), 9.8041(4), 18.9098(8)	17.862(4), 9.0804(18), 15.254(3)
α/°, β/°, γ/°	90, 98.445(4), 90	90, 94.289(2), 90	90, 99.06(3), 90
Volume / $Å^3$	1836.95(16)	2197.80(15)	2443.3(9)
Z	4	4	4
ρ_{calc} / mg mm^{-3}	1.525	1.665	2.015
μ / mm^{-1}	1.089	0.861	6.850
F(000)	876	1116	1432
Crystal size / mm^3	0.11 × 0.016 × 0.011	0.119 × 0.041 × 0.019	0.131 × 0.025 × 0.023
2Θ range for data collection	4.328 to 49.982°	3.92 to 59.098°	4.618 to 63.338°
Index ranges	$-20 \le h \le 20, 0 \le k \le 13, 0 \le l \le 11$	$-16 \le h \le 16, -13 \le k \le 13, -25 \le l \le 25$	$-26 \le h \le 22, -10 \le k \le 13, -19 \le l \le 22$
Reflections collected	3217	58364	31961
Independent reflections	3217[R(int) = 0.0454]	6038[R(int) = 0.0469]	8254[R(int) = 0.0520]
Data/restraints/parameters	3217/0/240	6038/0/400	8254/180/409
Goodness-of-fit on F^2	1.051	1.159	0.986
Final R indexes [I>2σ (I)]	$R_1 = 0.0499$, $wR_2 = 0.0812$	$R_1 = 0.0713$, $wR_2 = 0.1600$	$R_1 = 0.0281$, $wR_2 = 0.0539$

Final R indexes [all data]	R_1 = 0.0782, wR_2 = 0.0890	R_1 = 0.0942, wR_2 = 0.1698	R_1 = 0.0384, wR_2 = 0.0569
Largest diff. peak/hole / e $Å^{-3}$	0.592/-0.436	1.963/-0.753	1.183/-1.157

Table S3. Crystallographic Data for **4** and **5**.

	4	**5**
Empirical formula	$C_{68}H_{69}BClFeN_2OPPtS_2$	$C_{41}H_{41}B_2Cl_2F_8FeN_2PPtS_2$
Formula weight	1322.54	1152.31
Temperature / K	100.01	100.02
Crystal system	triclinic	triclinic
Space group	P-1	P-1
a / Å, b / Å, c / Å	11.0864(7), 12.6716(8), 23.6012(15)	9.755(2), 10.735(3), 20.825(5)
α/°, β/°, γ/°	86.285(3), 76.550(3), 68.456(3)	88.803(6), 79.374(7), 79.790(6)
Volume / $Å^3$	2998.6(3)	2109.4(9)
Z	2	2
ρ_{calc} / mg mm^{-3}	1.465	1.814
μ / mm^{-1}	2.758	3.990
F(000)	1344	1136
Crystal size / mm^3	0.117 × 0.062 × 0.055	0.277 × 0.184 × 0.014
2Θ range for data collection	3.456 to 61.13°	1.99 to 66.554°
Index ranges	$-15 \le h \le 15$, $-17 \le k \le 18$, $-33 \le l \le 31$	$-15 \le h \le 14$, $-15 \le k \le 16$, $-32 \le l \le 32$
Reflections collected	46366	80312
Independent reflections	18220[R(int) = 0.0438]	16044[R(int) = 0.0474]

Data/restraints/parameters	18220/0/706	16044/0/542
Goodness-of-fit on F^2	1.097	1.063
Final R indexes [I>2σ (I)]	R_1 = 0.0525, wR_2 = 0.1172	R_1 = 0.0305, wR_2 = 0.0790
Final R indexes [all data]	R_1 = 0.0591, wR_2 = 0.1203	R_1 = 0.0364, wR_2 = 0.0808
Largest diff. peak/hole / e $Å^{-3}$	5.550/-2.380	6.005/-1.523

Computational Studies

All structures were optimized at the ω-B97XD/lanl2dz level of theory. Functional ω-B97XD includes dispersion effects albeit empirically. The lanl2dz basis set includes a pseudopotential for heavy atoms (second row and beyond),[8] whereby the core electrons on these heavier atoms are replaced by a set of functions that simulate their presence and their effect on the valence electrons. This approach allows computational resources to be used instead for a higher quality description of the valence electrons and their interactions with surrounding units.[9] Interaction energies were calculated with the Natural Bond Orbital (NBO) deletion method and developed under the NBO population analysis. NBO allows for a localized, pairwise description of the electron density and is more reliable than the Mulliken's default. This takes the Fock matrix and finds the elements that connect orbitals from one atom to those of another and sets their values to zero (deletion); the resulting matrix is re-diagonalized and the associated energy value increases with respect to the original non-deleted one. The change in energy is ascribed to the interaction energy.[10-11]

The complexes with same surrogate ligands were superimposed onto each other and the corresponding root-mean square deviation of atomic positions (RMSD) values were calculated (Table S5). A large RMSD value denotes that the conformation of ligand changes significantly upon redox reaction. The superimposed energy-minimized models show that the change in orientation of Fc/Fc^+ group is responsible for the large RMSD values in **7**/**8** and **7-THT**/**8-THT** (Figure S30).

Molecular electrostatic potentials were calculated at the ω-B97XD/lanl2dz level of theory and mapped with the 0.02 e/Å^3 isodensity value (Figure S31). The oxidized complexes (Fe^{III}) are most electron poor at the Fe^{III} node (for **6**) or the Pt^{II} node (for **7** and **7-THT**).The small shift in electron density during the formation of **7** and **7-THT** from **6** is consistent with electronic stabilization of S-Fc^+ via ligand displacement.

The oxidized complexes have an odd electron count and thus require an unrestricted calculation with their electron density being separated into α and β spin. The corresponding HOMO and LUMO are denoted as HOMOαβ, LUMOαβ and LUMOβ respectively. For all the calculations HOMOα are qualitatively indistinguishable from HOMOβ and thus only one is shown as HOMOαβ. For the non-oxidized complexes, the HOMO resides on ferrocene, which is susceptible of being oxidized, whereas the LUMO are located on the organometallic fragment. Upon oxidation, however, the HOMOs reside on the organometallic fragment whereas the LUMOs are located on ferrocenium, which is susceptible of being reduced (Figure S32).

Table S4. Relative free energies (kcal/mol) and energy minimized models of **5**, **5***, **6** and **6***. Asterisk denotes the minor diastereomer of the fully closed complex.

Compound	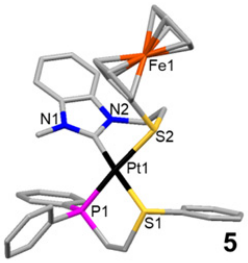 **5**	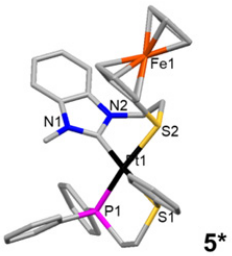 **5***
Relative free energy (kcal/mol)	0	1.592
Compound	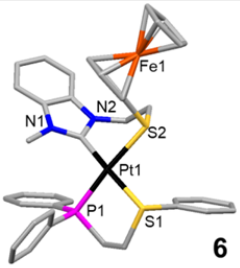 **6**	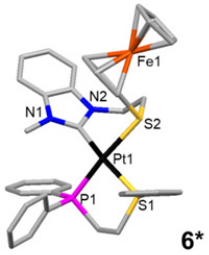 **6***
Relative free energy (kcal/mol)	0	3.103

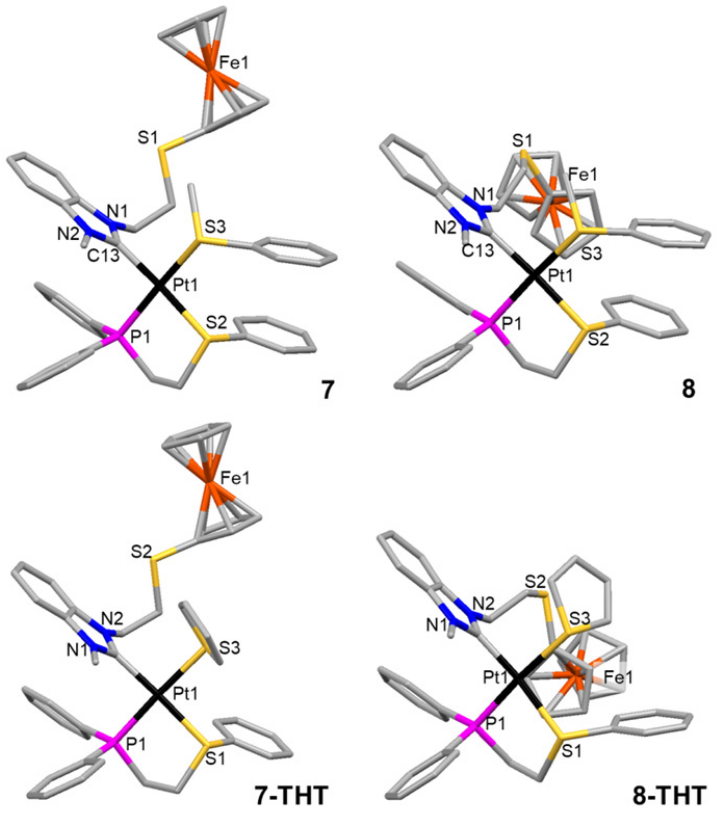

Figure S29. Energy minimized DFT models of **7**, **8**, **7-THT**, and **8-THT**.

Table S5. Calculated Pt–L bond energies (kcal/mol) and P1-Fe1 distances (Å).

Compound	L	Fe oxidation state	Bond Energy (kcal/mol)	P1-Fe1 distance (Å)	RMSD (Å)
5	N/A	II	66.22	7.592	0.267
6	N/A	III	60.56	7.732	
7	PhSMe	III	62.20	9.985	2.129
8	PhSMe	II	61.57	7.668	
7-THT	THT	III	56.25	9.933	2.949
8-THT	THT	II	51.39	6.714	

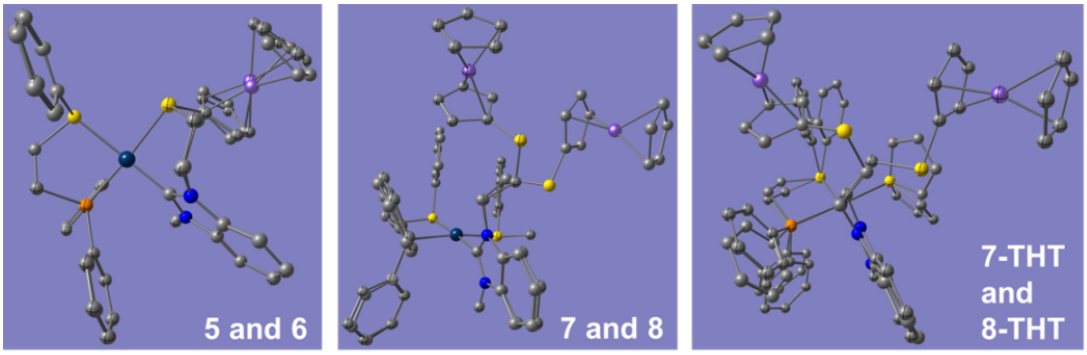

Figure S30. Superimposed energy-minimized models of the non-oxidized complex and its oxidized counterpart.

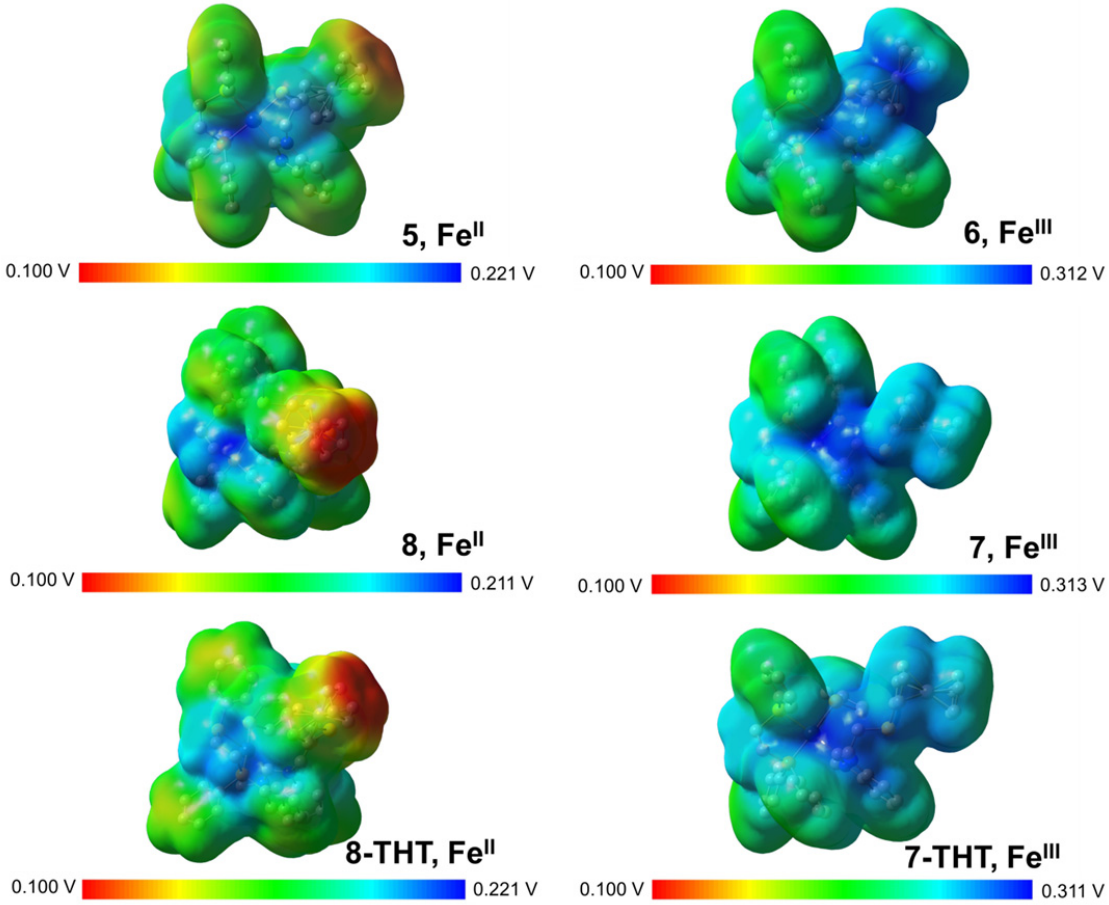

Figure S31. Electrostatic potential maps of **5**, **6**, **7**, **8**, **7-THT**, and **8-THT**. Regions of higher electron density are color coded red, and electron poor regions are color coded blue.

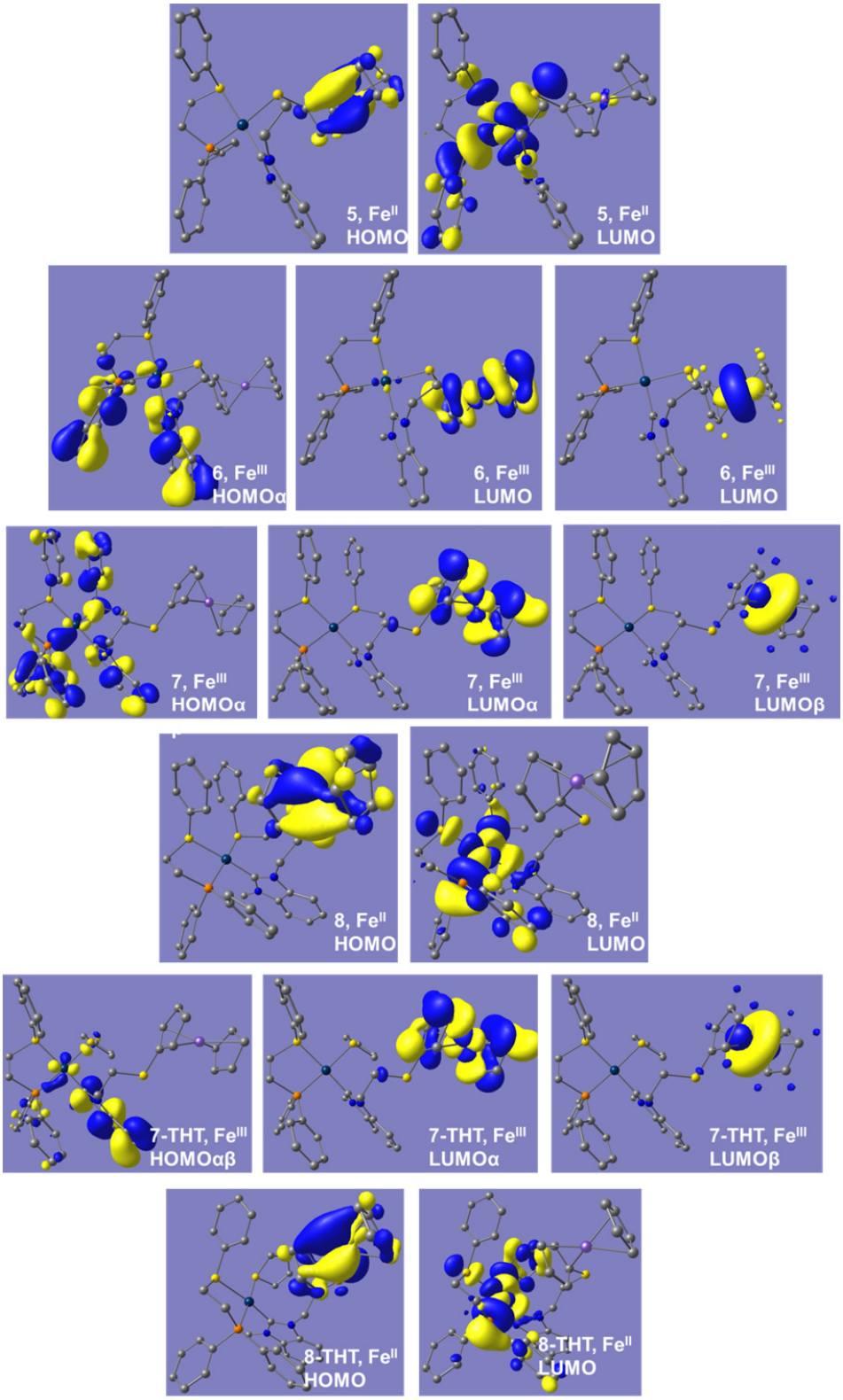

Figure S32. Frontier orbital maps of **5**, **6**, **7**, **8**, **7-THT**, and **8-THT**.

NMR Spectra

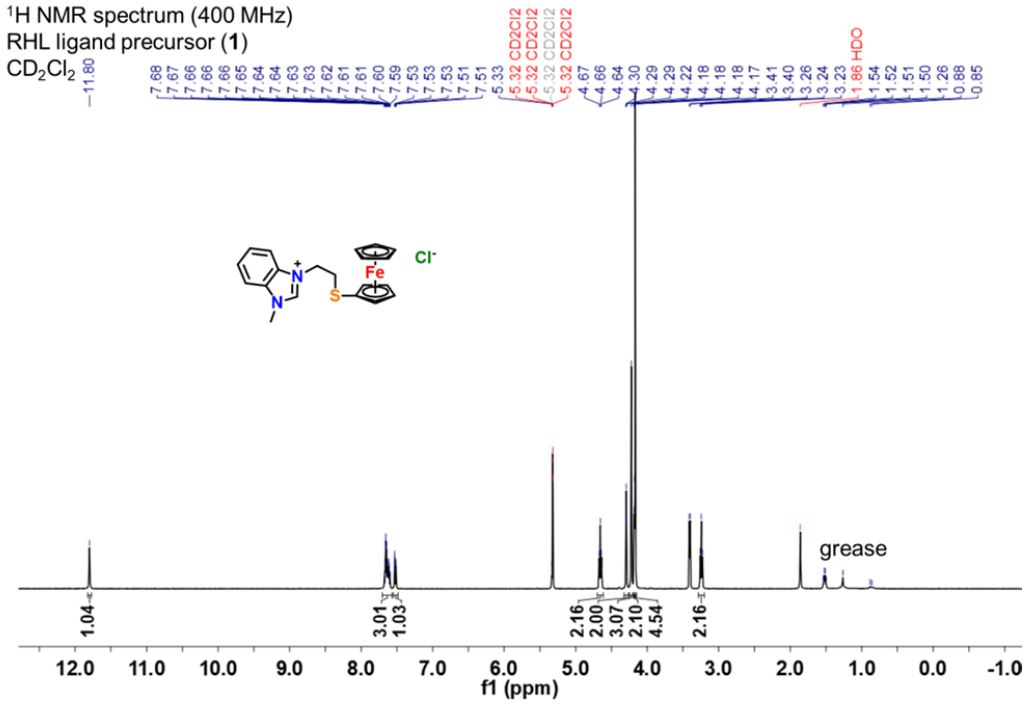

Figure S33. ^{1}H NMR (400 MHz, CD_2Cl_2, 298 K) spectrum of **1**.

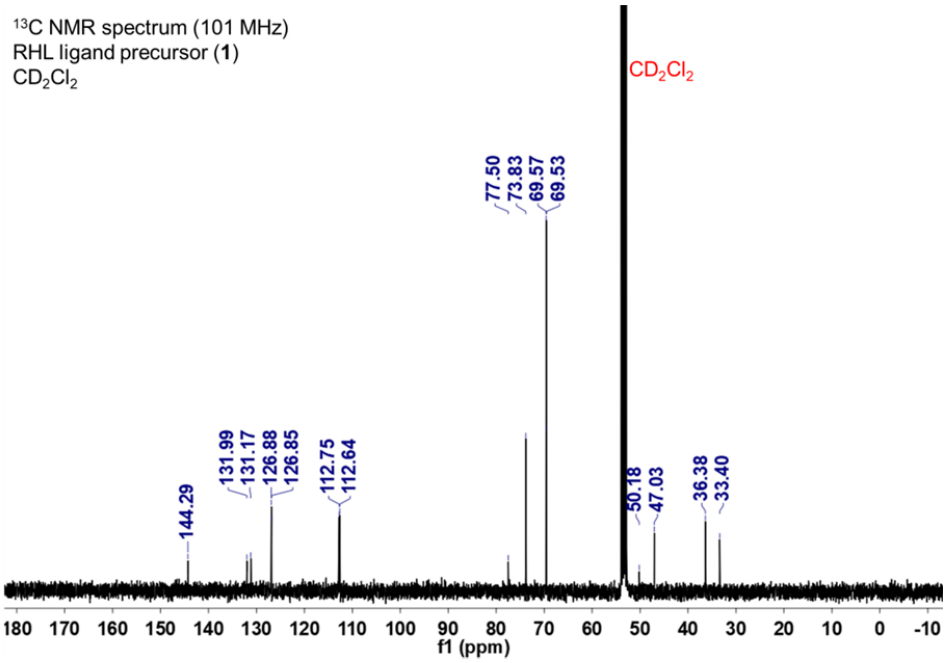

Figure S34. ^{13}C NMR (101 MHz, CD_2Cl_2, 298 K) spectrum of **1**.

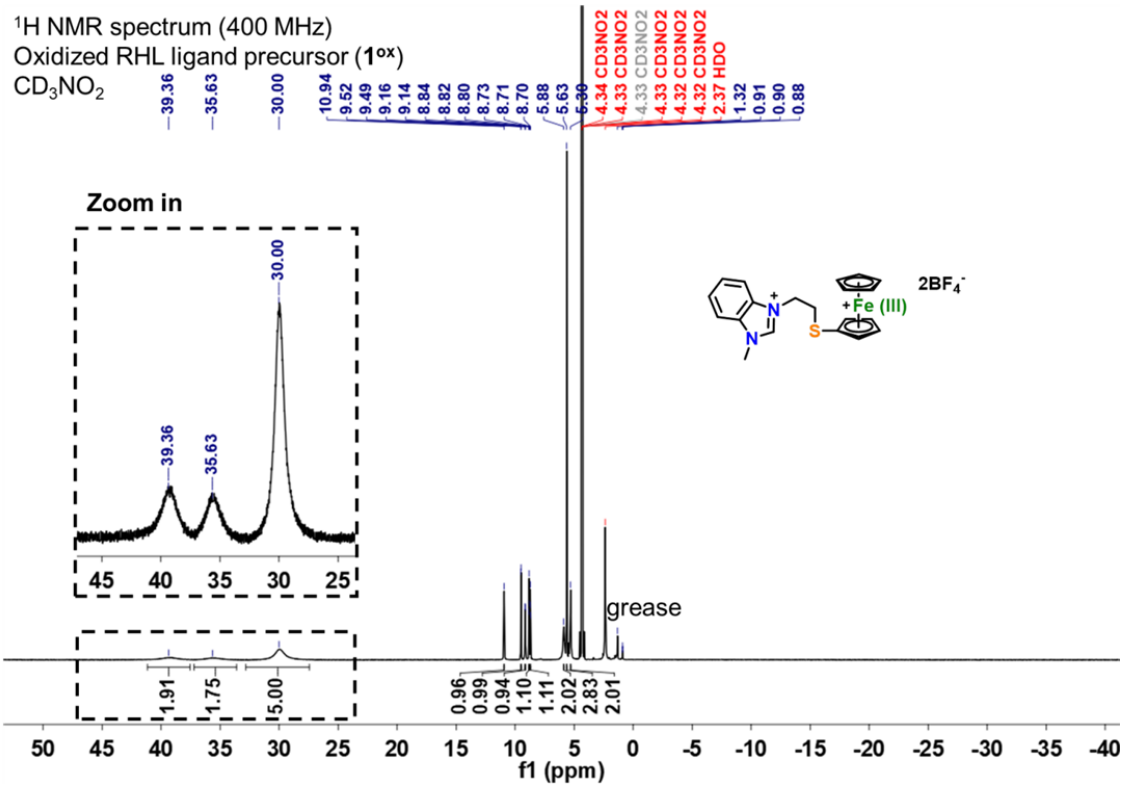

Figure S35. ^{1}H NMR (400 MHz, CD_3NO_2, 298 K) spectrum of **1^{ox}**.

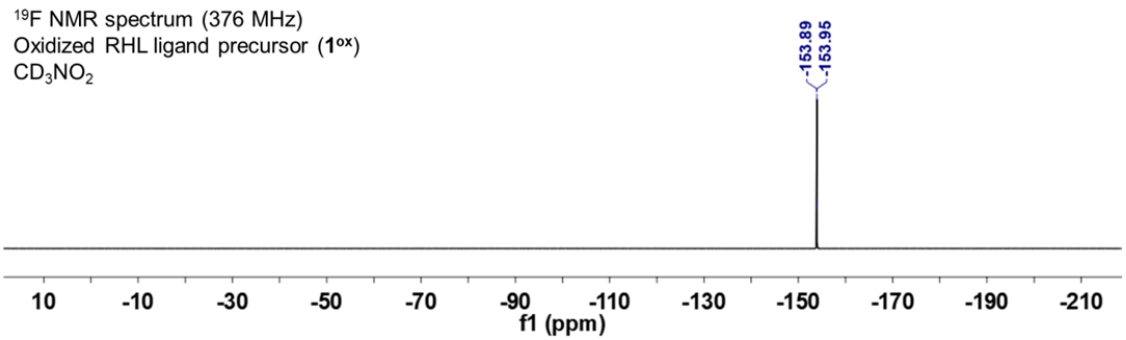

Figure S36. ^{19}F NMR (376 MHz, CD_3NO_2, 298 K) spectrum of **1^{ox}**.

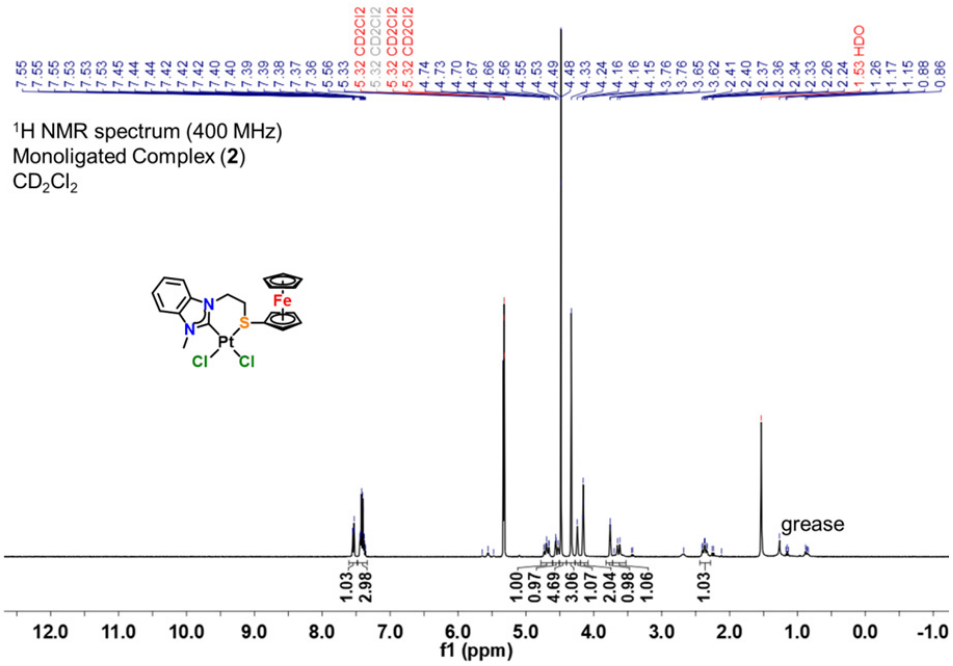

Figure S37. ^{1}H NMR (400 MHz, CD_2Cl_2, 298 K) spectrum of **2**.

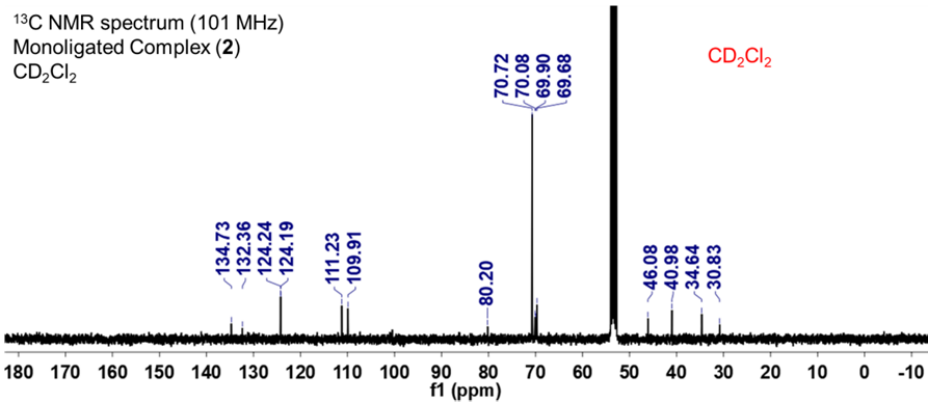

Figure S38. ^{13}C NMR (101 MHz, CD_2Cl_2, 298 K) spectrum of **2**.

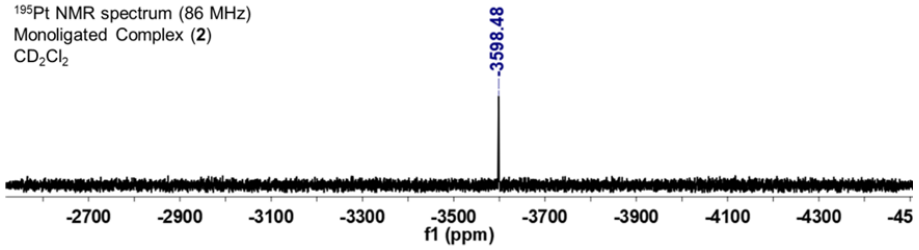

Figure S39. ^{195}Pt NMR (86 MHz, CD_2Cl_2, 298 K) spectrum of **2**.

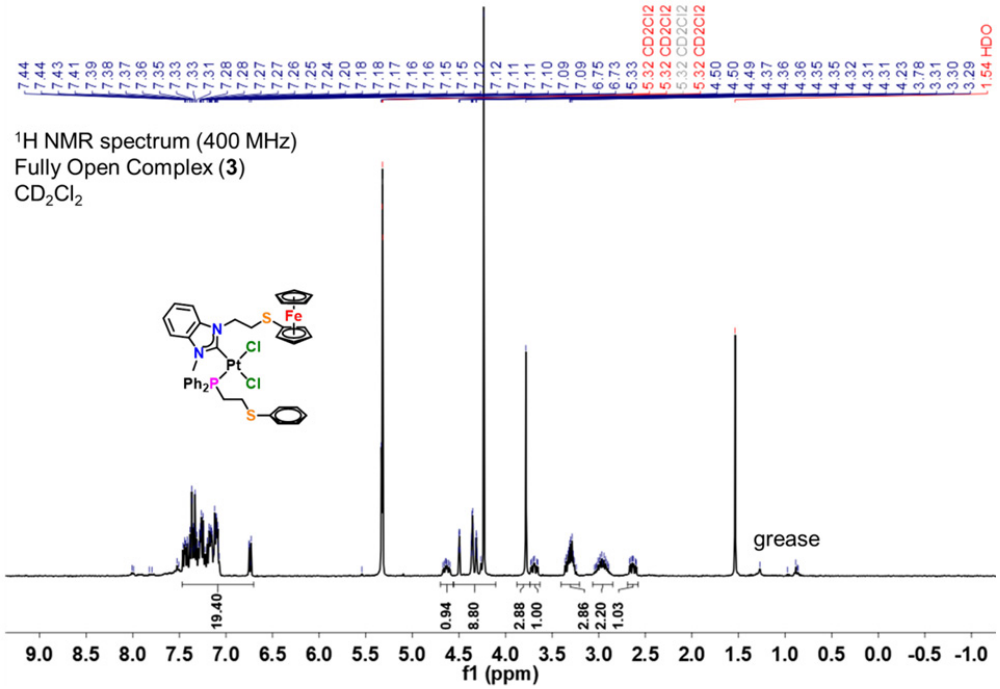

Figure S40. ^{1}H NMR (400 MHz, CD_2Cl_2, 298 K) spectrum of **3**.

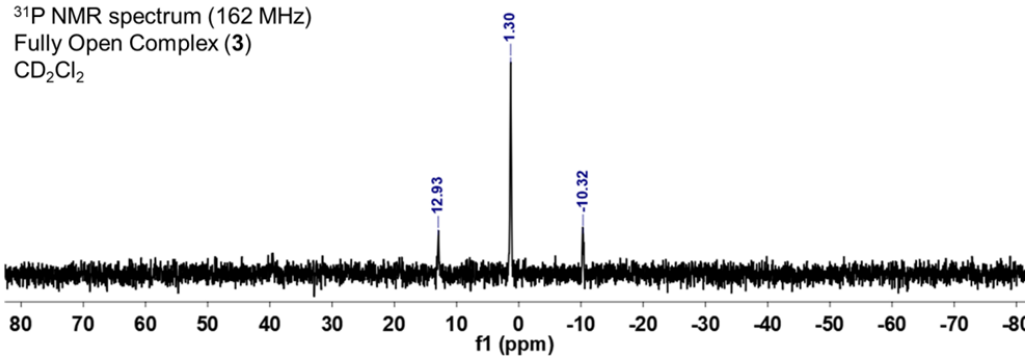

Figure S41. ^{31}P NMR (162 MHz, CD_2Cl_2, 298 K) spectrum of **3**.

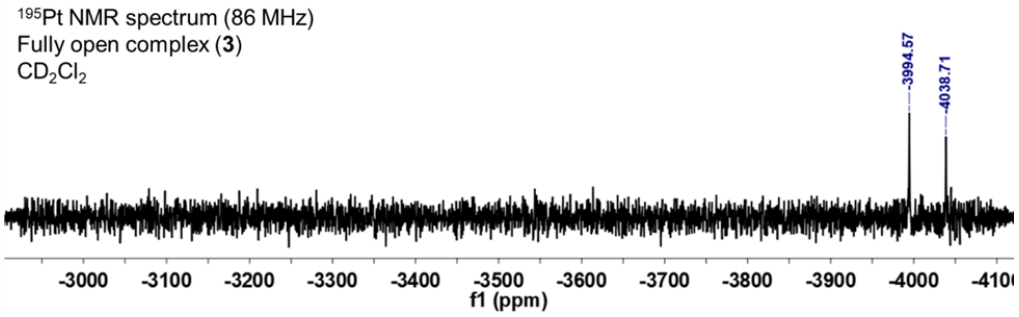

Figure S42. ^{195}Pt NMR (86 MHz, CD_2Cl_2) spectrum of **3** at 298 K.

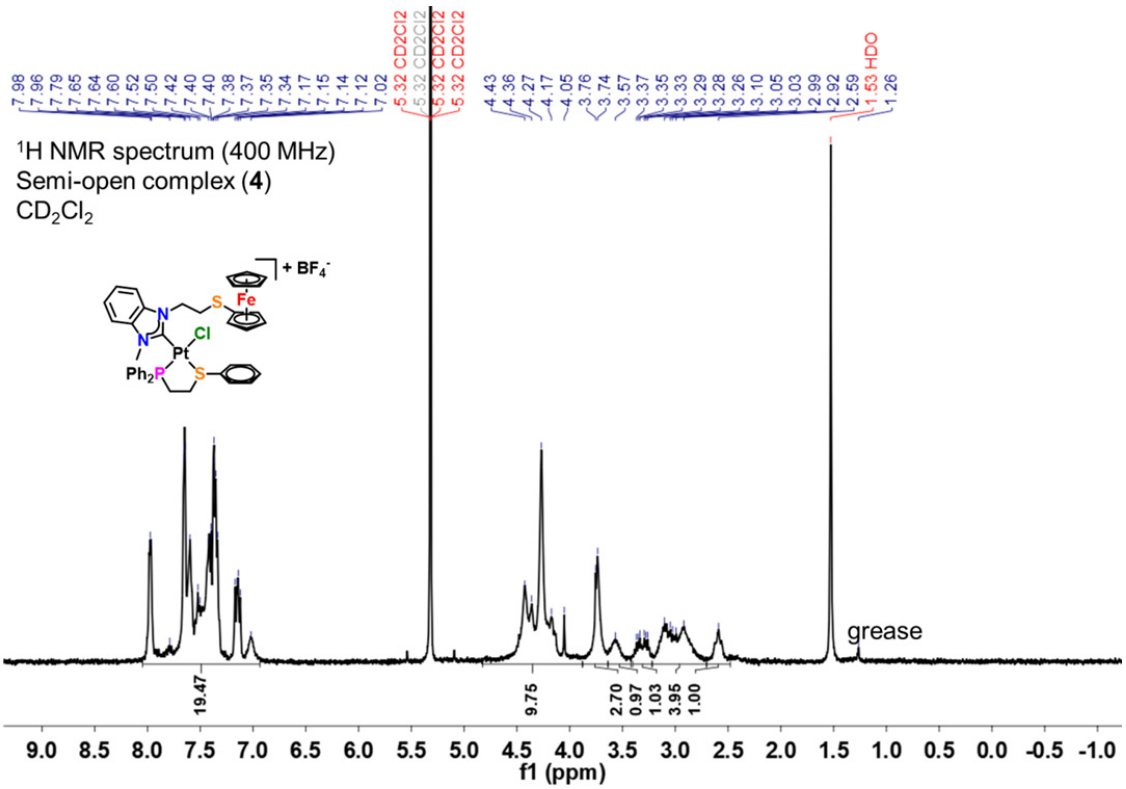

Figure S43. ^{1}H NMR (400 MHz, CD_2Cl_2, 298 K) spectrum of **4**.

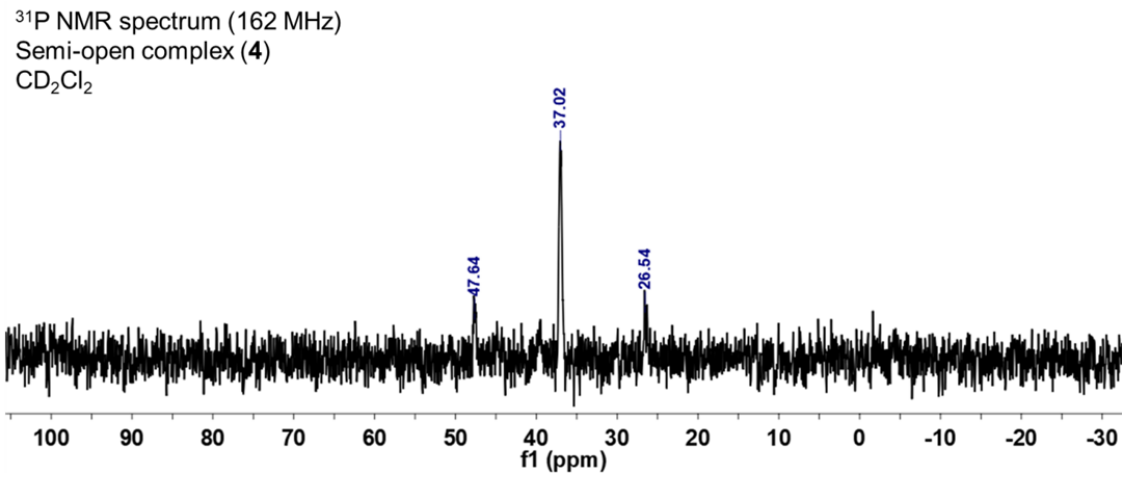

Figure S44. ^{31}P NMR (162 MHz, CD_2Cl_2, 298 K) spectrum of **4**.

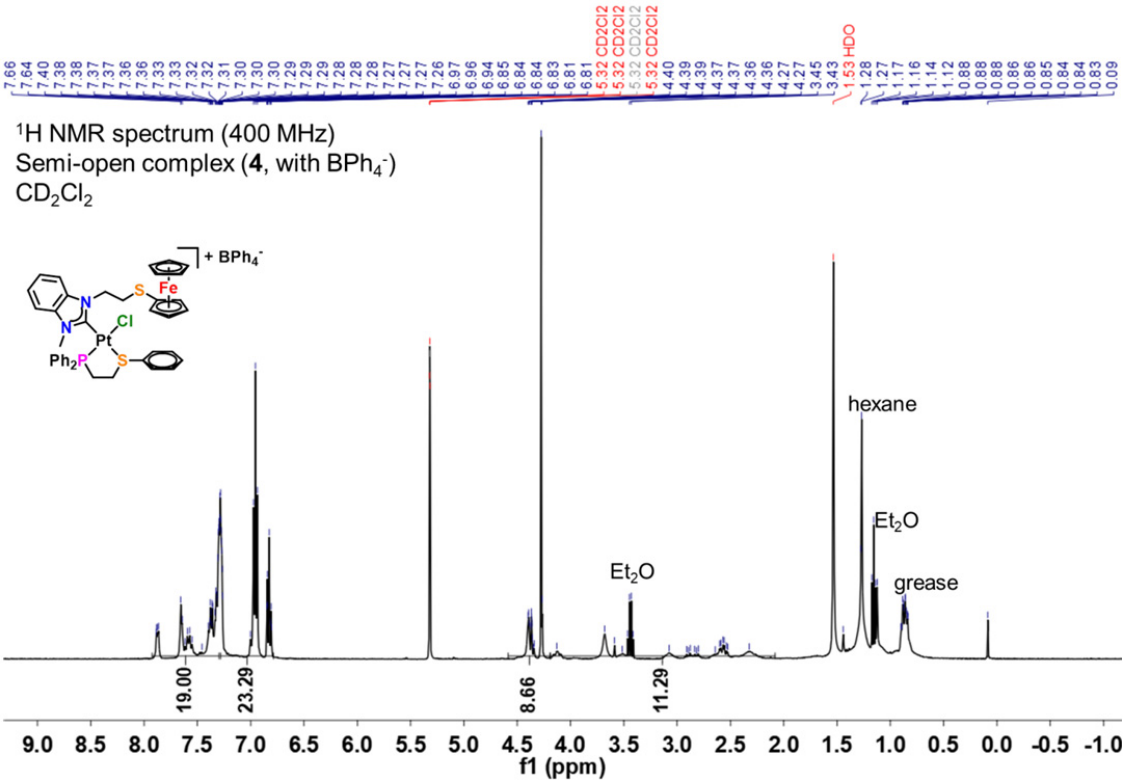

Figure S45. ^{1}H NMR (400 MHz, CD_2Cl_2, 298 K) spectrum of **4** (with BPh_4^-).

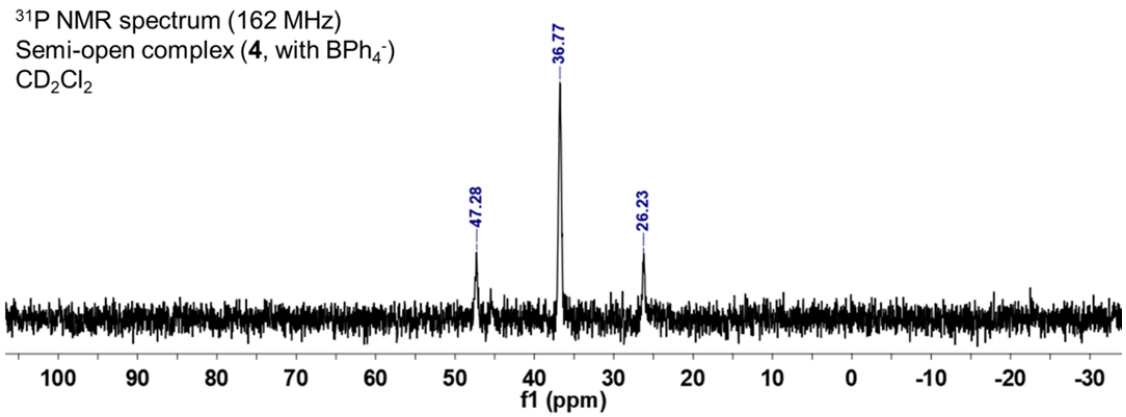

Figure S46. ^{31}P NMR (162 MHz, CD_2Cl_2, 298 K) spectrum of **4** (with BPh_4^-).

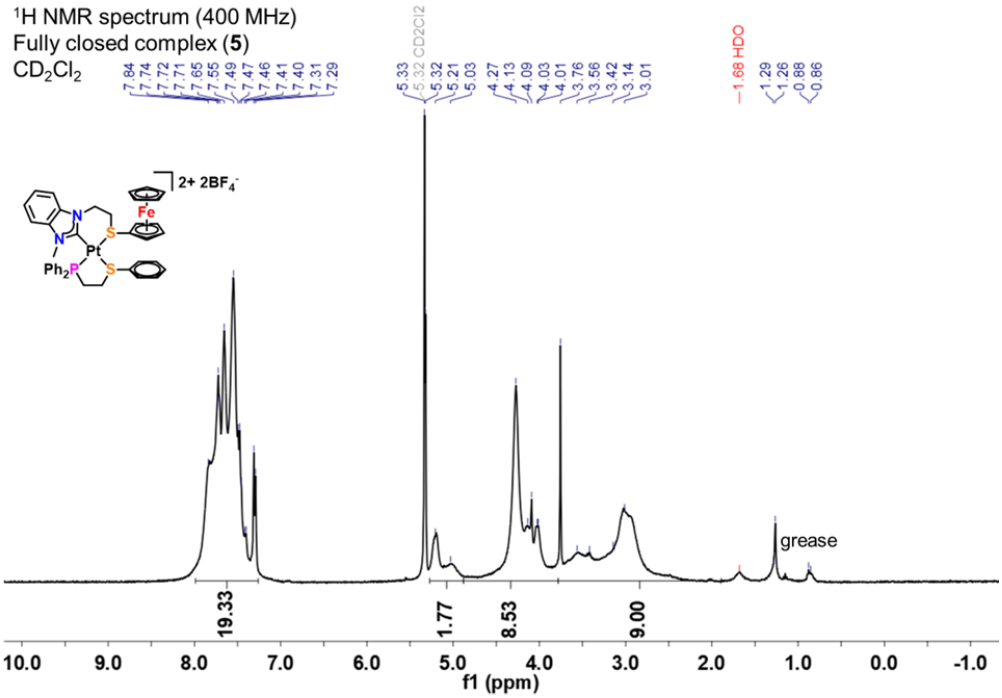

Figure S47. ^{1}H NMR (400 MHz, CD_2Cl_2, 298 K) spectrum of **5**.

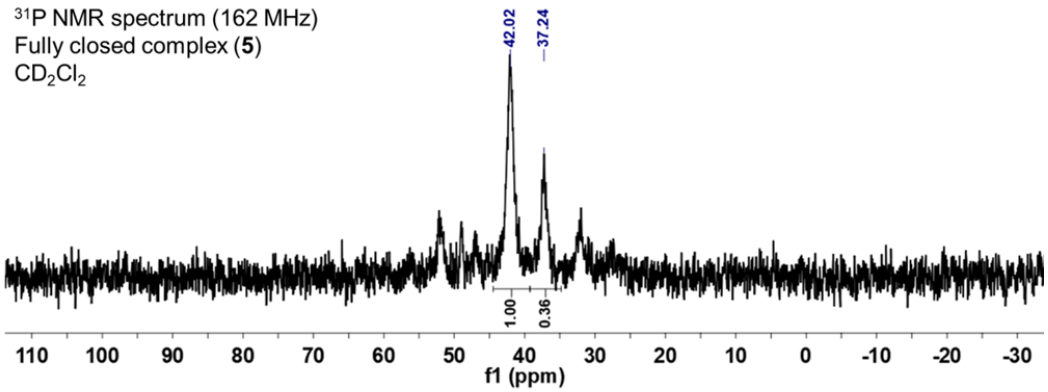

Figure S48. ^{31}P NMR (162 MHz, CD_2Cl_2, 298 K) spectrum of **5**.

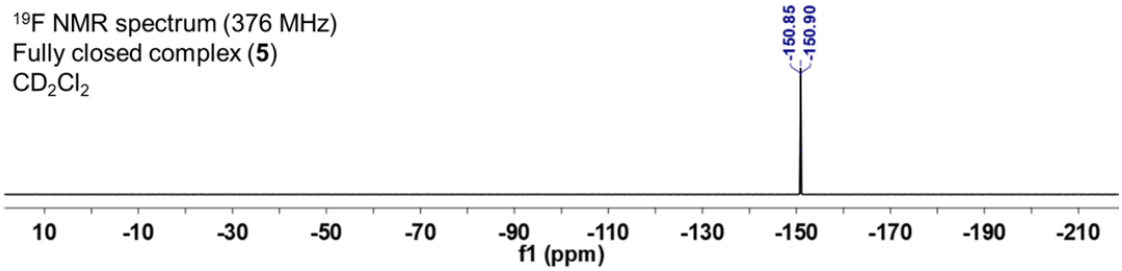

Figure S49. ^{19}F NMR (376 MHz, CD_2Cl_2, 298 K) spectrum of **5**.

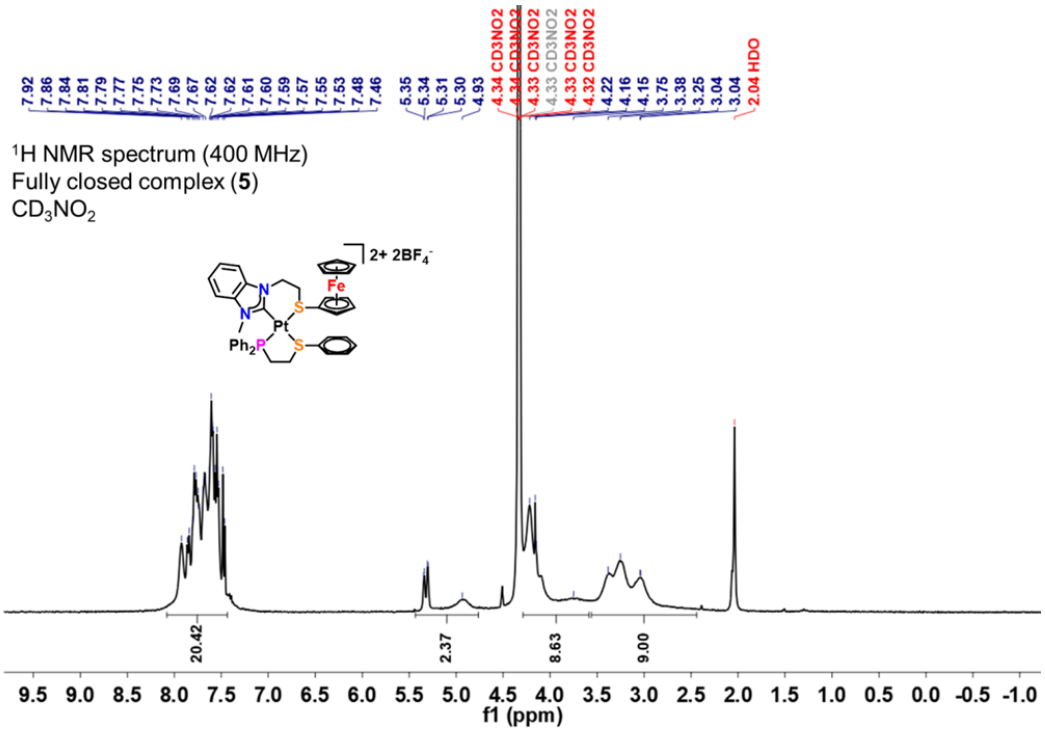

Figure S50. ^{1}H NMR (400 MHz, CD_3NO_2, 298 K) spectrum of **5**.

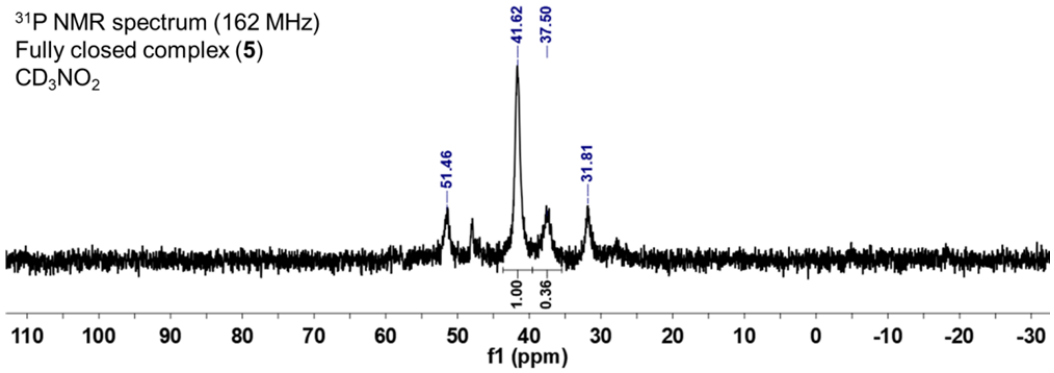

Figure S51. ^{31}P NMR (162 MHz, CD_3NO_2, 298 K) spectrum of **5**.

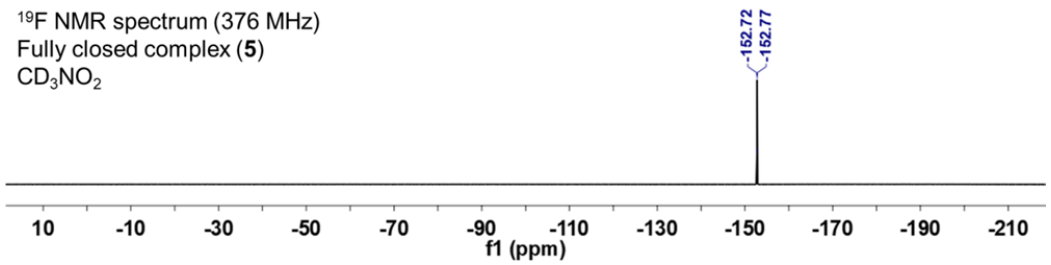

Figure S52. ^{19}F NMR (376 MHz, CD_3NO_2, 298 K) spectrum of **5**.

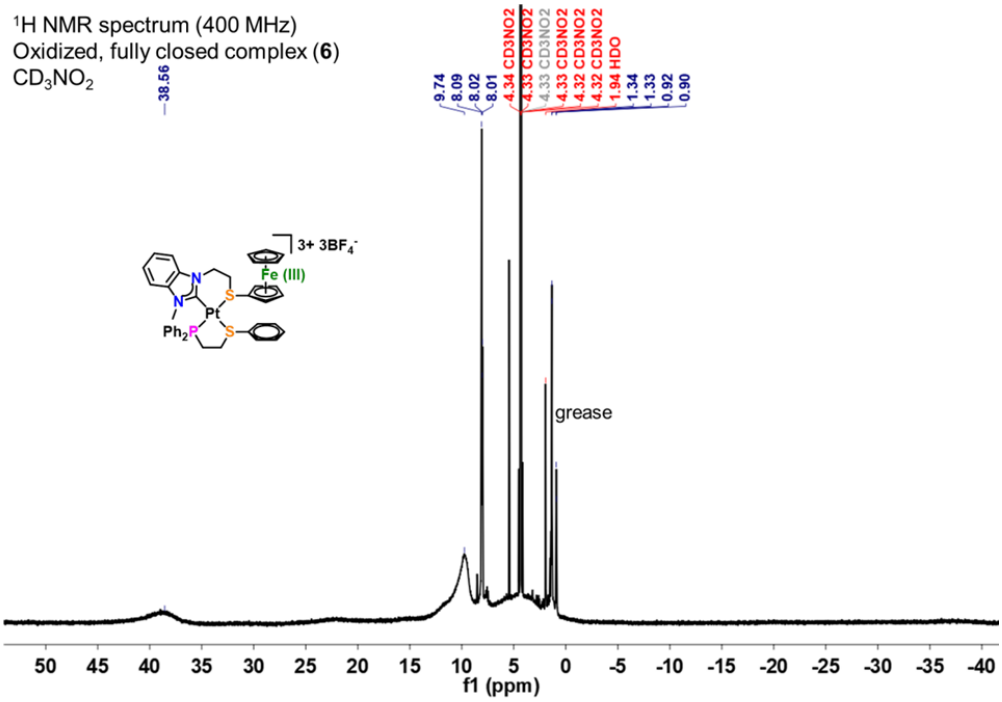

Figure S53. ^{1}H NMR (400 MHz, CD_3NO_2, 298 K) spectrum of **6**.

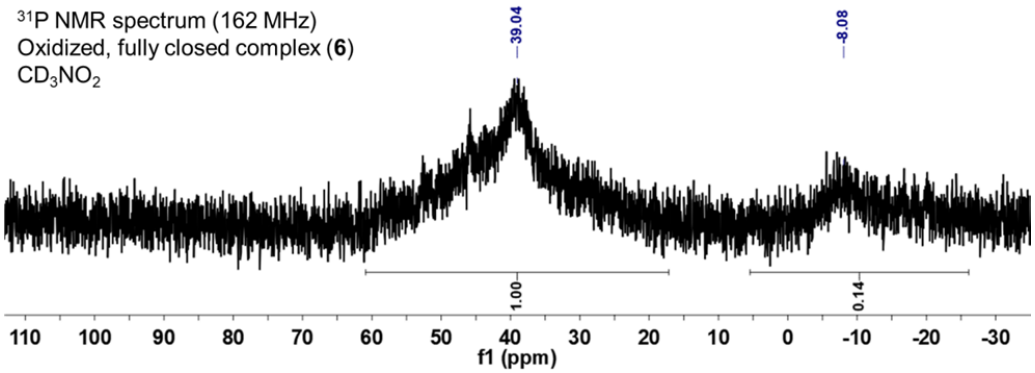

Figure S54. ^{31}P NMR (162 MHz, CD_3NO_2, 298 K) spectrum of **6**.

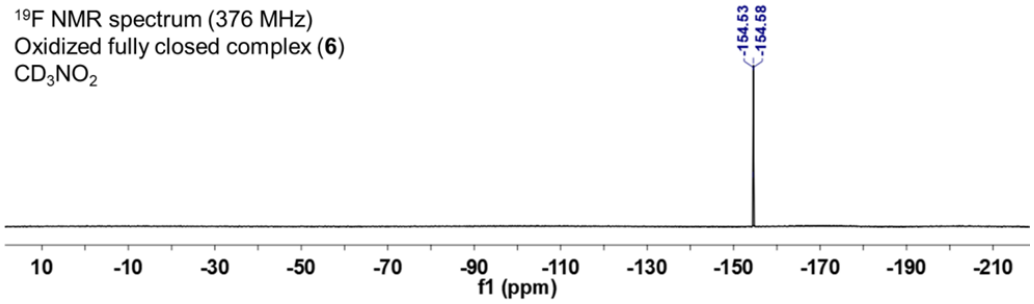

Figure S55. ^{19}F NMR (376 MHz, CD_3NO_2, 298 K) spectrum of **6**.

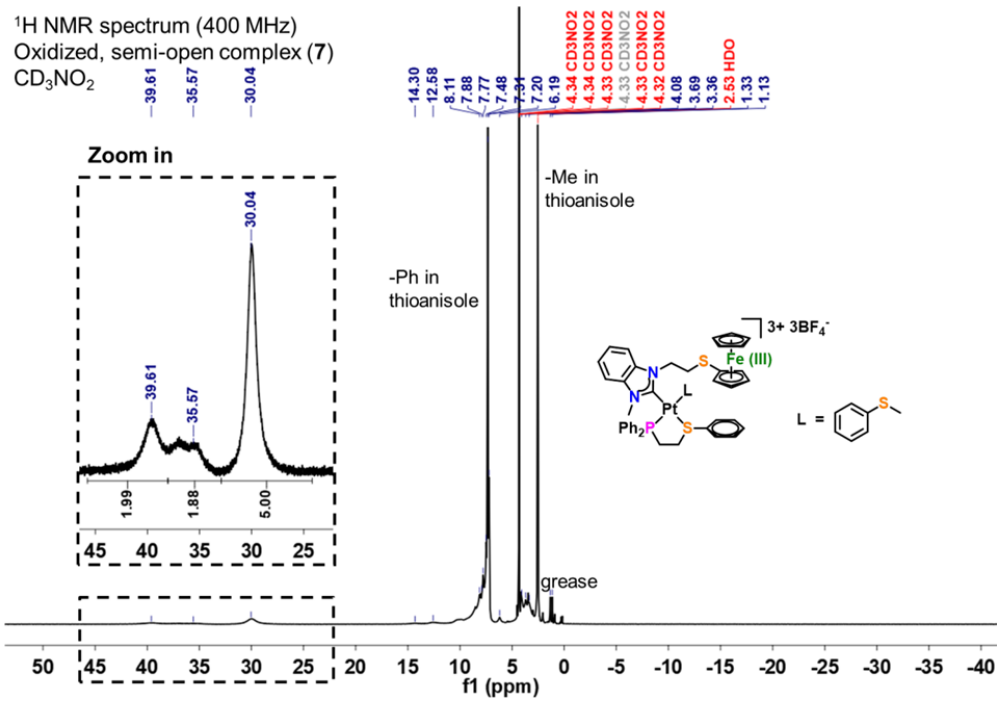

Figure S56. ^{1}H NMR (400 MHz, CD_3NO_2, 298 K) spectrum of **7**.

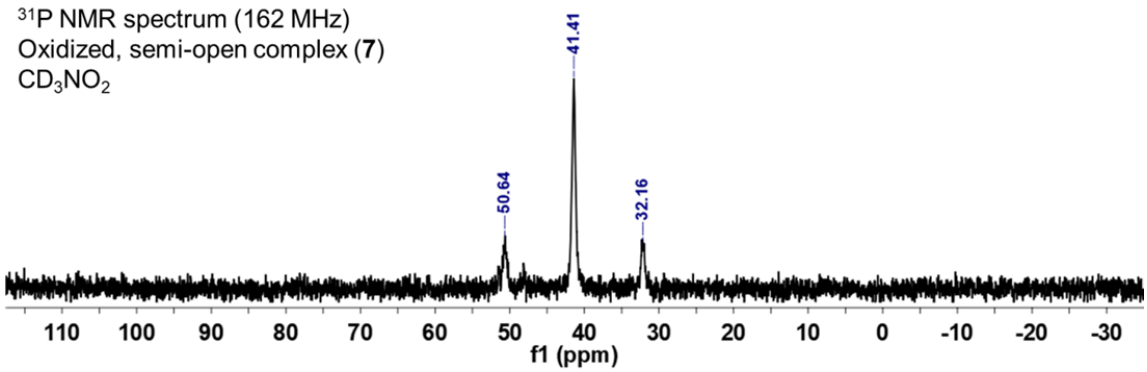

Figure S57. ^{31}P NMR (162 MHz, CD_3NO_2, 298 K) spectrum of **7**.

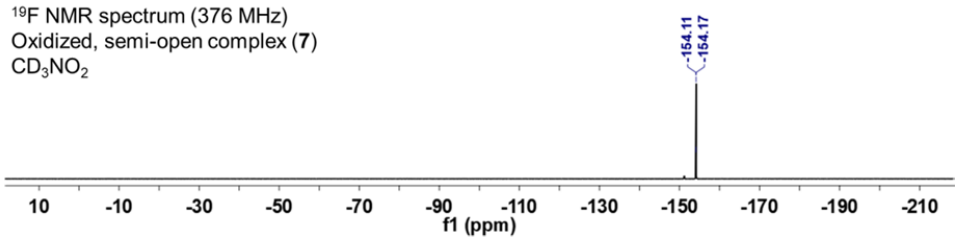

Figure S58. ^{19}F NMR (376 MHz, CD_3NO_2, 298 K) spectrum of **7**.

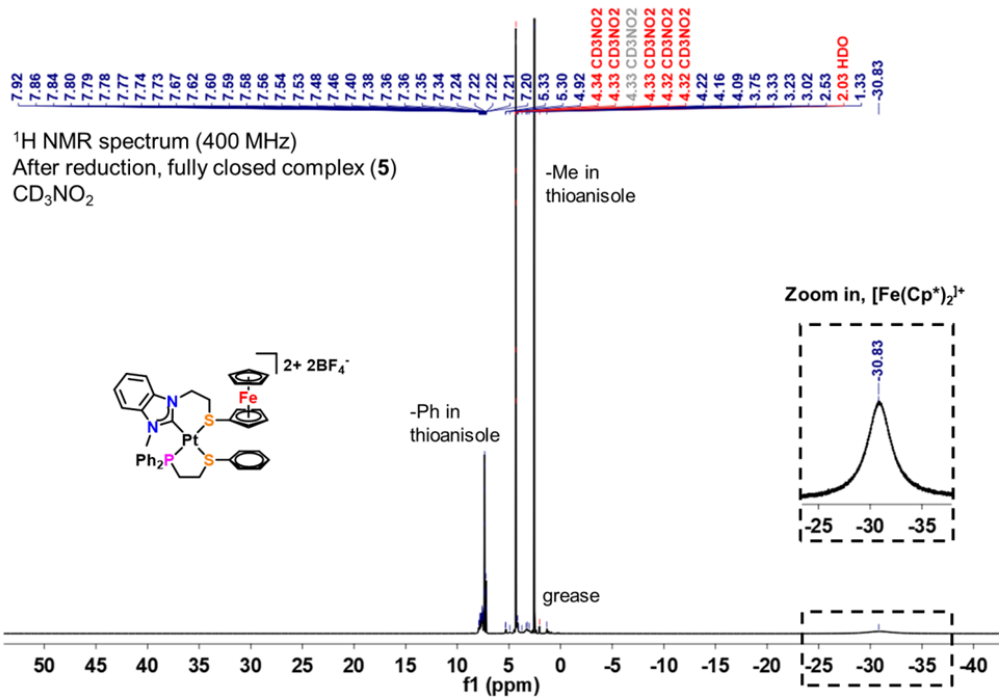

Figure S59. ^{1}H NMR (400 MHz, CD_3NO_2, 298 K) spectrum of **5**, formed from the reduction of complex **7**.

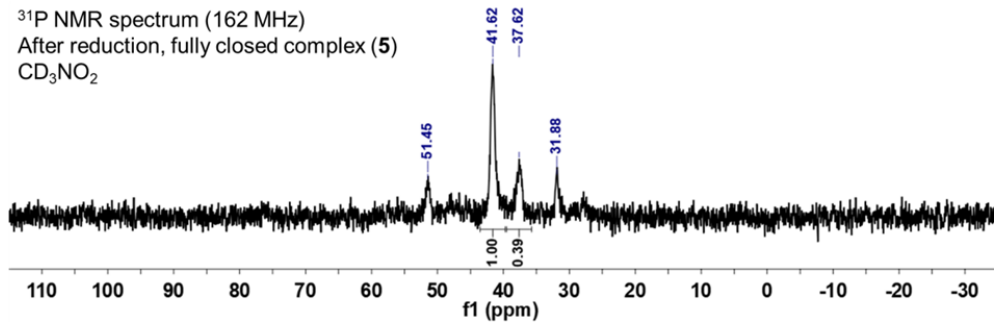

Figure S60. ^{31}P NMR (162 MHz, CD_3NO_2, 298 K) spectrum of **5**, formed from the reduction of complex **7**.

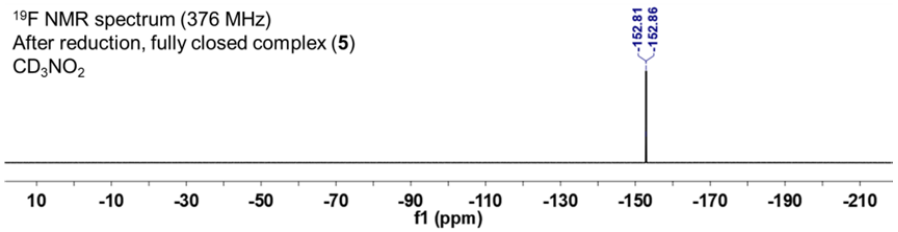

Figure S61. ^{19}F NMR (376 MHz, CD_3NO_2, 298 K) spectrum of **5**, formed from the reduction of complex **7**.

Mass Spectra

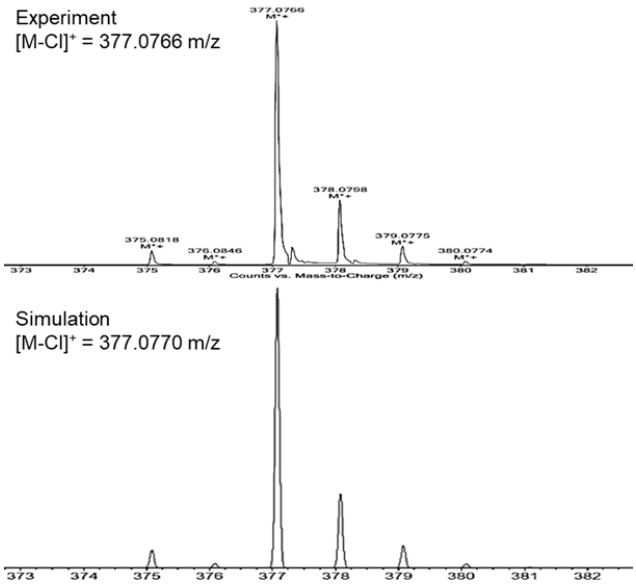

Figure S62. HRMS (ESI+) spectrum and the ISOPRO simulation of the molecular ion $[M-Cl]^+$ of **1**. Solvent: MeOH.

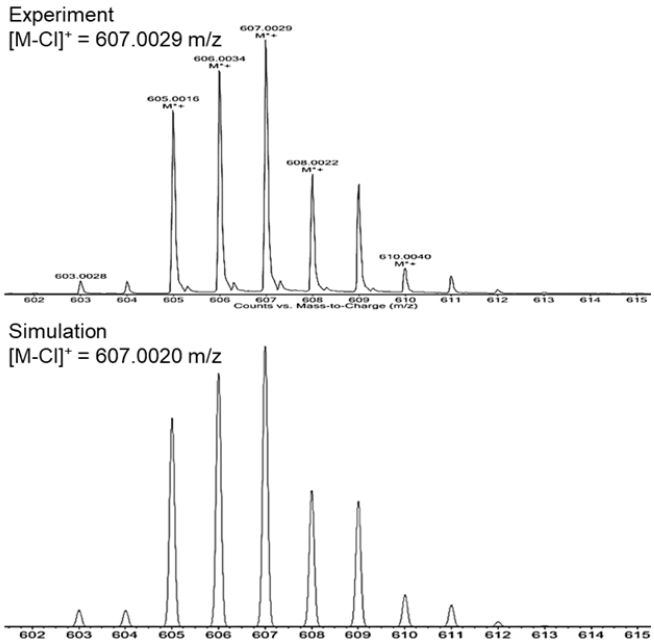

Figure S63. HRMS (ESI+) spectrum and the ISOPRO simulation of the molecular ion $[M-Cl]^+$ of **2**. Solvent: MeOH.

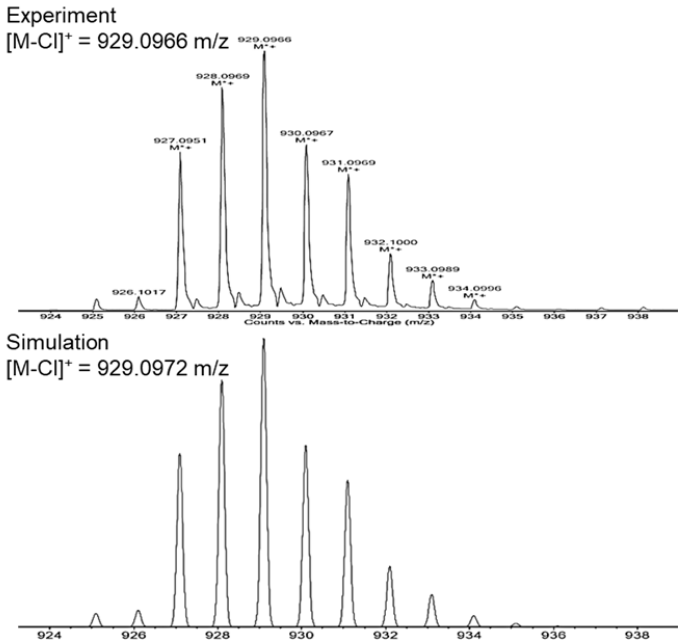

Figure S64. HRMS (ESI+) spectrum and the ISOPRO simulation of the molecular ion $[M-Cl]^+$ of **3**. Solvent: MeOH.

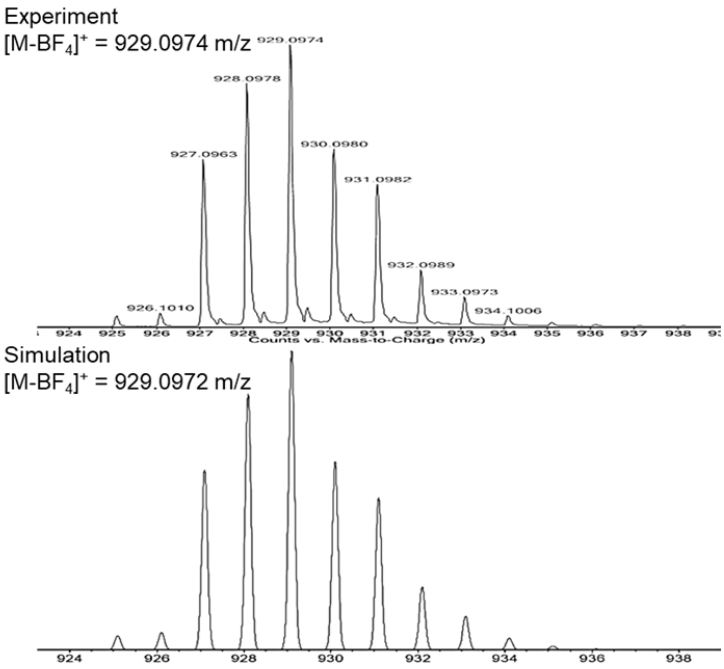

Figure S65. HRMS (ESI+) spectrum and the ISOPRO simulation of the molecular ion $[M-BF_4]^+$ of **4**. Solvent: MeOH.

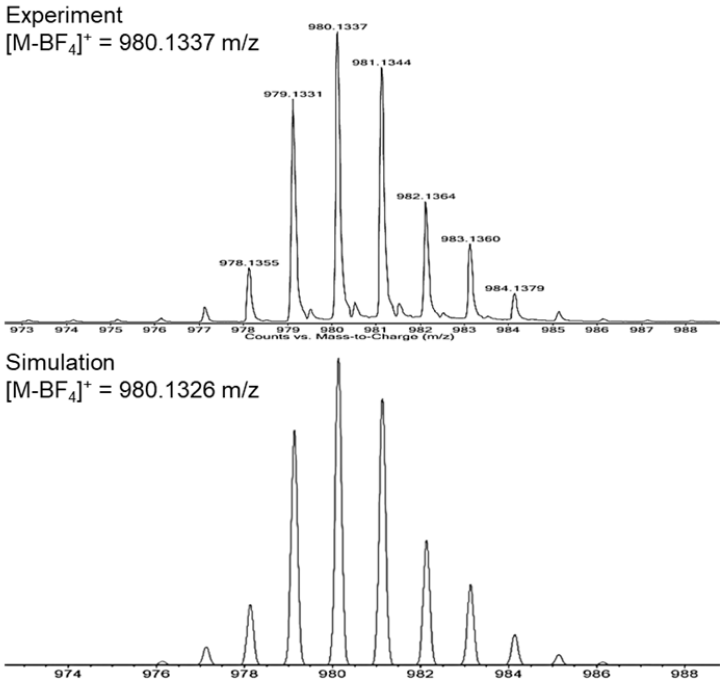

Figure S66. HRMS (ESI+) spectrum and the ISOPRO simulation of the molecular ion $[M-BF_4]^+$ of **5**. Solvent: MeOH.

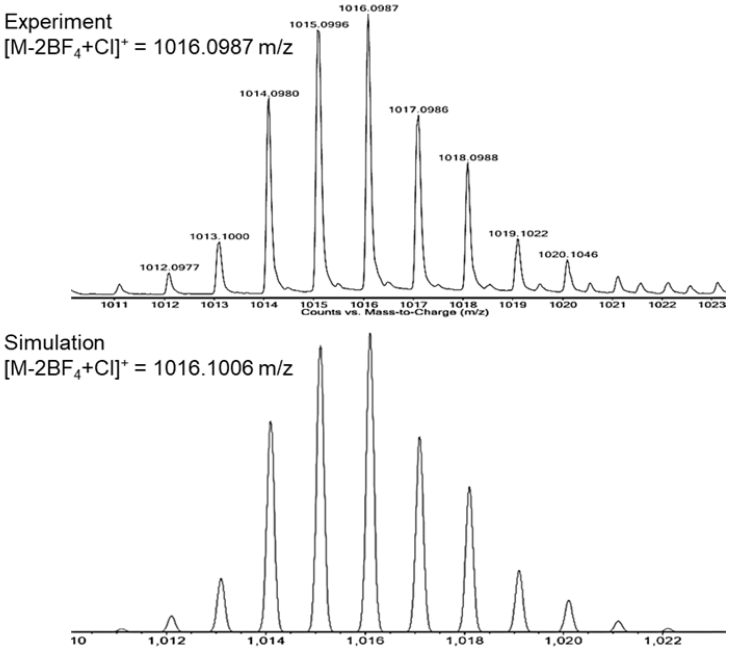

Figure S67. HRMS (ESI+) spectrum and the ISOPRO simulation of the molecular ion $[M-2BF_4+Cl]^+$ of **6**. Solvent: CH_2Cl_2/CH_3NO_2.

References

(1) Kourkine, I. V.; Slone, C. S.; Mirkin, C. A.; Liable-Sands, L. M.; Rheingold, A. L., Small Molecule-Induced Intramolecular Electron "Pitch and Catch" in a Rhodium(I) Complex with Substitutionally Inert Redox-Active Ligands. *Inorg. Chem.* **1999**, *38*, 2758-2759.

(2) Garrou, P. E., ΔR-ring contributions to phosphorus-31 NMR parameters of transition-metal-phosphorus chelate complexes. *Chem. Rev.* **1981**, *81*, 229-266.

(3) Barriere, F.; Geiger, W. E., Use of Weakly Coordinating Anions to Develop an Integrated Approach to the Tuning of ΔE1/2 Values by Medium Effects. *J. Am. Chem. Soc.* **2006**, *128*, 3980-3989.

(4) Thordarson, P., Determining association constants from titration experiments in supramolecular chemistry. *Chem. Soc. Rev.* **2011**, *40*, 1305-1323.

(5) Dolomanov, O. V.; Bourhis, L. J.; Gildea, R. J.; Howard, J. A. K.; Puschmann, H., OLEX2: a complete structure solution, refinement and analysis program. *J. Appl. Crystallogr.* **2009**, *42*, 339-341.

(6) Sheldrick, G. M., SHELXT - Integrated space-group and crystal-structure determination. *Acta Crystallogr., Sect. A: Found. Adv.* **2015**, *71*, 3-8.

(7) Sheldrick, G. M., Crystal structure refinement with SHELXL. *Acta Crystallogr., Sect. C: Struct. Chem.* **2015**, *71*, 3-8.

(8) Hay, P. J.; Wadt, W. R., Ab initio effective core potentials for molecular calculations. Potentials for the transition metal atoms scandium to mercury. *J. Chem. Phys.* **1985**, *82*, 270-283.

(9) Cundari, T. R.; Benson, M. T.; Lutz, M. L.; Sommerer, S. O., Effective core potential approaches to the chemistry of the heavier elements. *Rev. Comput. Chem.* **1996**, *8*, 145-202.

(10) Wesenberg, G.; Weinhold, F., Coupling of internal rotations in propanelike molecules. *Int. J. Quantum Chem.* **1982**, *21*, 487-509.

(11) Weinhold, F.; Landis, C. R., *Discovering Chemistry With Natural Bond Orbitals*. Wiley: Hoboken, N.J., 2012.